of the field-of-view (FOV). PET scanning was performed in 2-D mode. Following a 10-min transmission scan using a rotating external ^{68}Ge-^{68}Ga rod source, 18F-solution of approximately 37 MBq was inserted into the grey matter compartment of the phantom. PET scan was carried out for 10 min. Images were reconstructed using a standard Filtered-Back Projection (FBP) using a Hunning Filter, with standard correction procedures for random, detector normalization, attenuation, and scatter. Eight-millimetre postfilter also applied.

Data analysis

X-ray CT and SPECT images were registered to the digital design images of the phantom. The agreement with the X-ray CT images was visually analyzed for all five phantoms, particularly the agreement of fine structures of the cortex regions, the presence of residual resin materials in grey matter and bone compartments, and smoothness of the inner phantom surface or local distortion. It was also analyzed whether air bubbles were left in the grey matter or bone compartments on for the experiments filling both compartments with liquid.

Digital design images for the grey matter were extracted and were smoothed using a 3-dimensional Gaussian filter so as to match the spatial resolution of each of SPECT and PET images. The agreement between the SPECT and PET images acquired with the ^{99m}Tc and ^{123}I, and ^{18}F solutions; the digital design images were visually evaluated.

Three ROIs were placed on the attenuation coefficient images obtained from the ^{99m}Tc rod source-based transmission scan, namely the brain region, skull region, and whole head contour as carried out in our earlier study on young healthy volunteers [2, 15, 16]. The averaged attenuation coefficient values were obtained for each of these three ROIs and were compared with the values obtained for the young healthy subjects.

All data are presented as the mean ± 1 SD. Student's t test was used to evaluate the difference, and $p < 0.05$ was considered statistically significant.

Results

The results from the phantom assessment are summarized in Table 1. The volume of the skull component was 306.0 ± 1.9 mL, which was consistent with the expected volume of this component calculated as a summation of the surface area at each slice times the slice interval (305.6 mL). However, the grey matter volume was 562.2 ± 0.9 mL, which is 11.6 mL (2.1 %) greater than the estimated value of 550.6 mL. The phantom height was 212.7 ± 0.1 mm, and the weight of the phantom, excluding the internal liquid, was 1996.8 ± 1.9 g. It is important to note that once the phantom was filled with water, the weight becomes heavier than the original weight. It required more than a day to remove water inside the compartments so that the weight becomes closer to the original value <5 g.

Figure 3a, b shows example X-ray CT images of a phantom without and with filling liquid into the compartments, respectively. Both images were aligned and re-sliced to match to the digital design images shown in Fig. 2. Note that X-ray CT images demonstrated a high contrast in the bone area due to K_2HPO_4 solution, and slightly reduced contrast in the grey matter area compared to the polymer resin areas. The visual analysis showed no particular distortion of the fine structure or resin materials remaining inside the compartments, as were also in other 4 phantoms. It was also confirmed that there were no apparent differences among the five phantoms on the X-ray CT images. No air bubbles were visible in either component.

The results of the attenuation coefficient values measured by the transmission scan using a SPECT camera are summarized in Table 2, along with values observed in healthy young volunteers in a previous study using the same procedures [2]. The attenuation values observed were 0.168 ± 0.006, 0.161 ± 0.006 and 0.206 ± 0.008 cm^{-1}, corresponding to the value averaged over the whole head contour at the slice indicating the maximum cross section, the cortical grey matter region and the skull (bone) region,

Table 1 Physical assessment of five pieces of the 3-dimensional brain phantom. The volume of the bone space essentially agreed with the designed parameter, but the grey matter region had a significantly greater value by 11.6 mL (2.1 %)

	#Phantom	Grey vol (mL)	Bone vol (mL)	Weight (g)	Height (mm)
1	1	564	303	1999	212.80
1	2	562	307	1996	212.80
2	3	563	308	1994	212.62
2	4	562	306	1998	212.69
2	5	562	306	1997	212.67
	Mean ± SD	562.6 ± 0.9	306.0 ± 1.9	1996.8 ± 1.9	212.7 ± 0.1
	Ideal value	550.6 mL	305.6 mL		

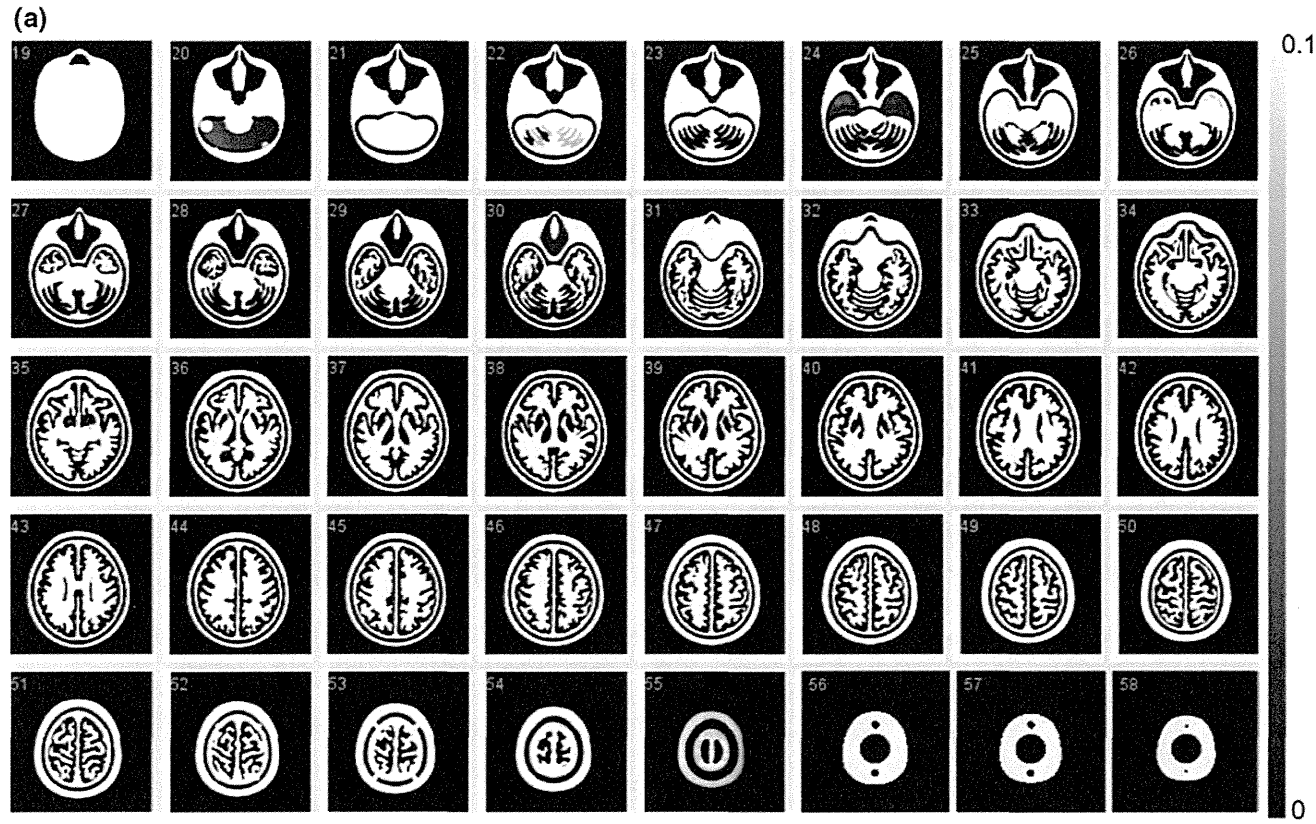

Fig. 3 **a** X-ray CT image of the developed phantom, which does not contain water or bone-equivalent liquid inside the phantom. Note that the images are converted to attenuation μ value with a peak value of 0.10 (cm^{-1}). The images are aligned to the digital design shown in Fig. 2. No remaining materials or irregular surface are seen inside the grey matter or bone compartments of the phantom. **b** X-ray CT images of a phantom that contains water in the grey matter region, and a K_2HPO_4 solution in the bone compartment. Note that the images are converted to attenuation μ value with a peak value of 0.20 (cm^{-1}). The images are aligned to the digital design of Fig. 2. There are no air bubbles remaining in the phantom

respectively. These values were similar to those from the healthy volunteers determined by the same criteria in our earlier study, which were 0.166 ± 0.01, 0.155 ± 0.007 and 0.197 ± 0010 cm^{-1}, respectively.

Figure 4 shows simulated images of the phantom, which represent only the grey matter component, without and with a 3-dimensional Gaussian filter that corresponded to the spatial resolution of the reconstructed SPECT images. Although homogeneous counts are assumed over the entire grey matter regions, the smoothed images (16 mm FWHM) represent inhomogeneous distribution. Figure 5 shows reconstructed SPECT images of the phantom, in which the grey matter component was filled with the ^{99m}Tc and ^{123}I solution, and the bone compartment was filled with the K_2HPO_4 liquid. The images, reconstructed using the QSPECT software including the attenuation, scatter correction using the attenuation coefficient images generated by means of the edge detection on the SPECT image, demonstrated reasonable agreement with the simulated images shown in Fig. 4 for both ^{99m}Tc and ^{123}I. Detailed structure is identical including the left–right asymmetrical distribution as follows; the counts in the occipital lob region as indicated in (a) are attributed to the thicker structure of the grey matter in this region, and the small spots indicated by (a–d) arrows are attributed to the presence of the cortical fissure. Images were also similar between the ^{99m}Tc and ^{123}I images.

Results from PET experiments are also compared with the simulated digital images in Fig. 6. Images showed good agreement with the digital design after smoothing with a Gaussian filter of 9 mm FWHM.

Figure 7 demonstrates the effects of applying a different magnitude of 3-dimensional Gaussian filter to the simulated phantom images that contain radioactivity only in the grey matter compartment. A greater amount of smoothing filter resulted in a reduced high-to-low contrast of the phantom images. Note that a particular part of the structure vanishes, and other regions become a cluster, by increasing the FWHM. It can be seen that relative contrasts in the phantom images vary dependent on the magnitude of 3-dimensional smoothing factor, largely attributed to the grey matter structure on the 3-dimensional domain.

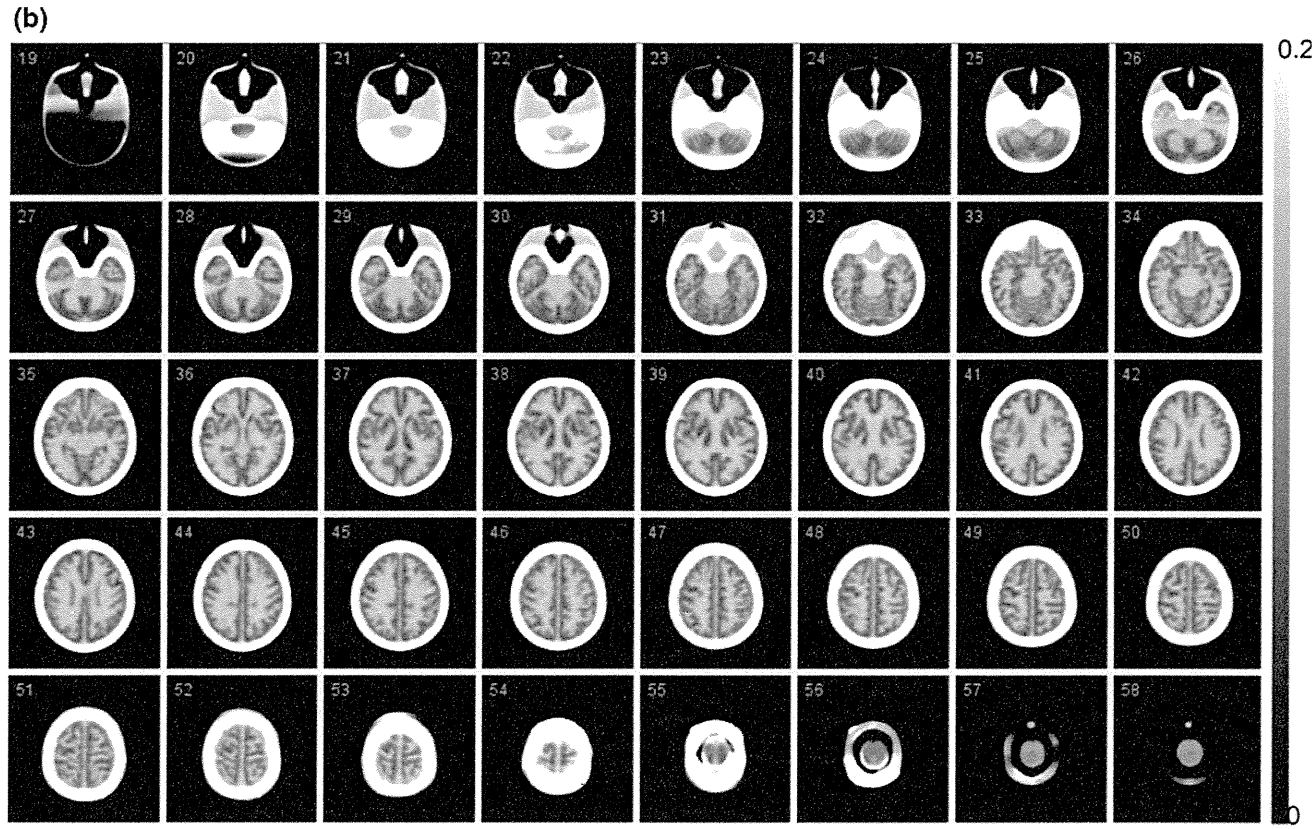

Fig. 3 continued

Table 2 Results of attenuation μ values for the averaged brain, cerebral region, and bone region that were obtained with the ^{99m}Tc-based transmission assessment

	μ values (cm^{-1})	
	Phantom	Human
Averaged over head	0.168 ± 0.006	0.166 ± 0.010
Cerebral tissue	0.161 ± 0.006	0.155 ± 0.007
Bone	0.206 ± 0.008	0.197 ± 0010

Discussion

This study demonstrated that the photo-curable laser-modelling technique, using the hydrophobic resin, can be used to construct a 3-dimensional brain phantom containing a fine grey matter structure with a detailed head contour and skull-equivalent and trachea components. With careful attention during the manufacturing process, the constructed phantoms appeared to be reasonably reproducible and agreed with the digital design within the accuracy of our image-registration technique. The supporting structures in the inner spaces, which have been the need in typical manufacturing process, could have been well avoided, providing smooth, non-distorted structure inside the grey-matter and skull compartments. The optimized procedures, including the decreased manufacturing speed during the laser-beam construction, pitch selection, and temperature, appeared to be adequate to ensure the solidity and reproducibility of the phantom.

As shown in Table 1, the variation in the volumes was ±0.2 % (or 0.9 mL) and ±0.6 % (or 1.9 mL), corresponding to the grey matter and skull regions, respectively. The total weight and height were also reproducible with variations of ±0.1 % and ±0.05 %, respectively. The attenuation coefficients of the phantom (Table 2), which were obtained using a ^{99m}Tc-rod source transmission measurement, were equivalent to those in healthy volunteers, which were assessed using the same experimental procedures in our earlier study for the whole brain, the cerebral tissue area, and the skull area [2]. This is because the photo-curable material used in this study has a similar attenuation coefficient and density (1.07 g/mL) compared to those of the human brain. The X-ray CT images shown in Fig. 3a, b demonstrated a good agreement with the digital design of the phantom shown in Fig. 2. More importantly, there were no residual resin materials on the X-ray CT images, nor any irregular inner wall surface of the phantom in the grey matter or bone compartments. The photo-curable laser-modelling technique usually requires supporting bridges (or pillar structures) when designing

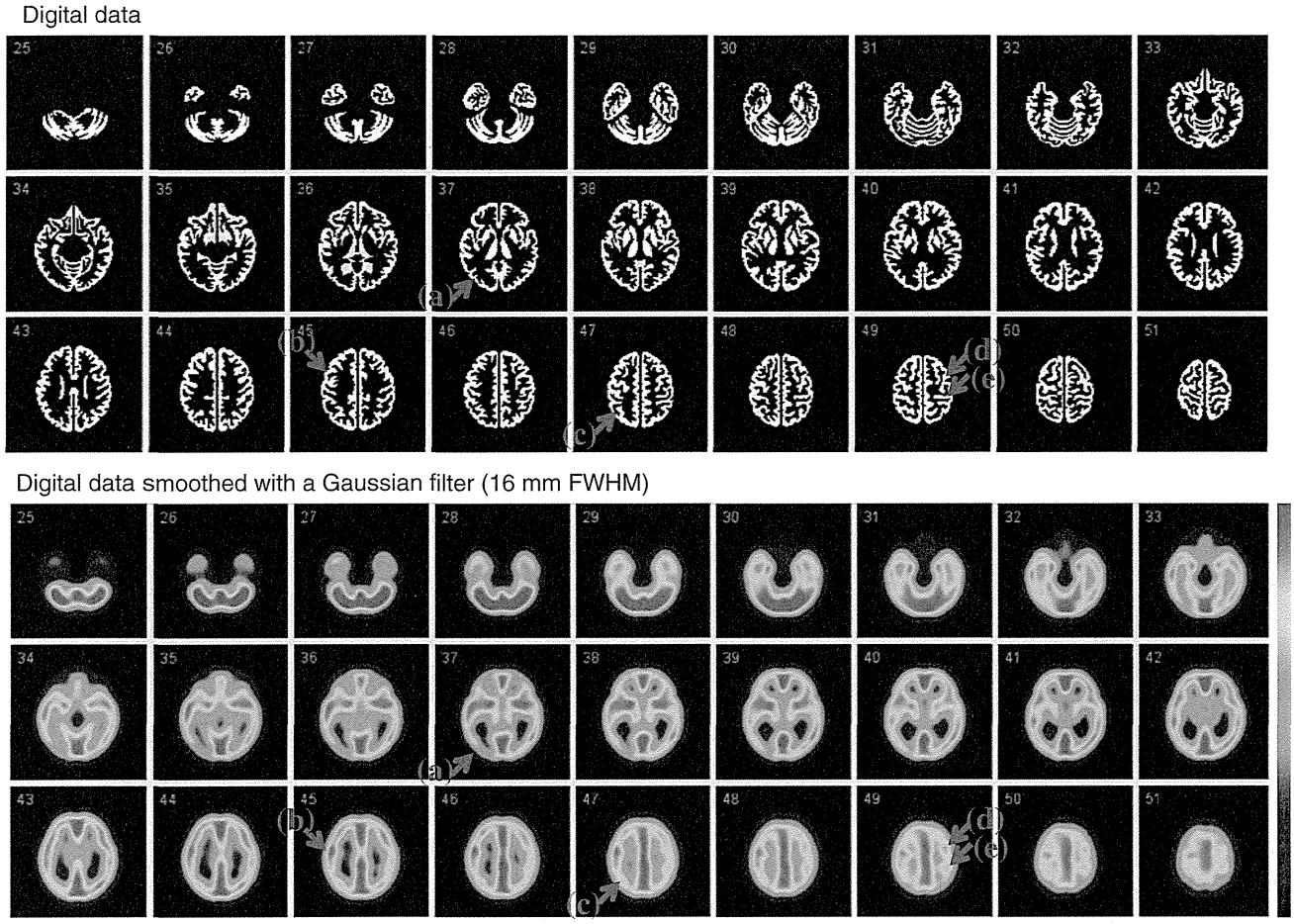

Fig. 4 Digital design of the grey matter area of the phantom in the original form (*top*) and after a smoothing operation with a Gaussian Filter of 16-mm full-width at half maximum (*bottom*), which corresponds to the spatial resolution of the SPECT images shown in Fig. 7. Note that the digital design data are noted with unity and null values, corresponding to the grey matter and other regions, respectively

structures in the horizontal direction. Our efforts of choosing optimal manufacturing procedures including the reduced speed, temperature and pitch, appeared to be feasible in order to remove such a supporting structure, which is essential in this 3-dimensional brain phantom. It is also important to note that the air bubbles could be well removed relatively easily from both the grey matter and bone compartments due to the connectivity of the liquid space.

In this phantom, we used a bone-equivalent solution of K_2HPO_4 as suggested in an earlier study [14]. This solution is known to have similar photon absorption coefficient values with bone or hydroxylapatite for a wide photon energy range, e.g., from 60 to 600 keV. This enables the applicability of this phantom even to the X-ray CT-based attenuation correction assessment. Use of this phantom also for PET acquisition with the energy of 511 keV is also valid. It should be noted that K_2HPO_4 is water soluble, and the solution could be concentrated until absorption coefficient values become greater than that of the human bone, while hydroxyapatite is not water-soluble. The water-soluble attenuation material is advantageous.

Of the note is that the SPECT images of the 3-dimensional brain phantom were consistent with the digital design of the phantom for both ^{99m}Tc and ^{123}I, after applying a Gaussian filter that corresponded to the spatial resolution of the reconstructed images. This is attributed to the accurate reconstruction software (QSPECT) [2, 17], including adequate attenuation- and scatter-correction procedures, employed in this study [2, 17]. The identical images between the ^{99m}Tc and ^{123}I isotopes further suggest the adequacy of the compensation procedures for penetration from high-energy photons emitted from the ^{123}I isotope itself [2, 17]. PET images reconstructed with the standard FBP procedures including the detector normalization, random, attenuation, and scatter correction processes were in a good agreement with the smoothed digital design images.

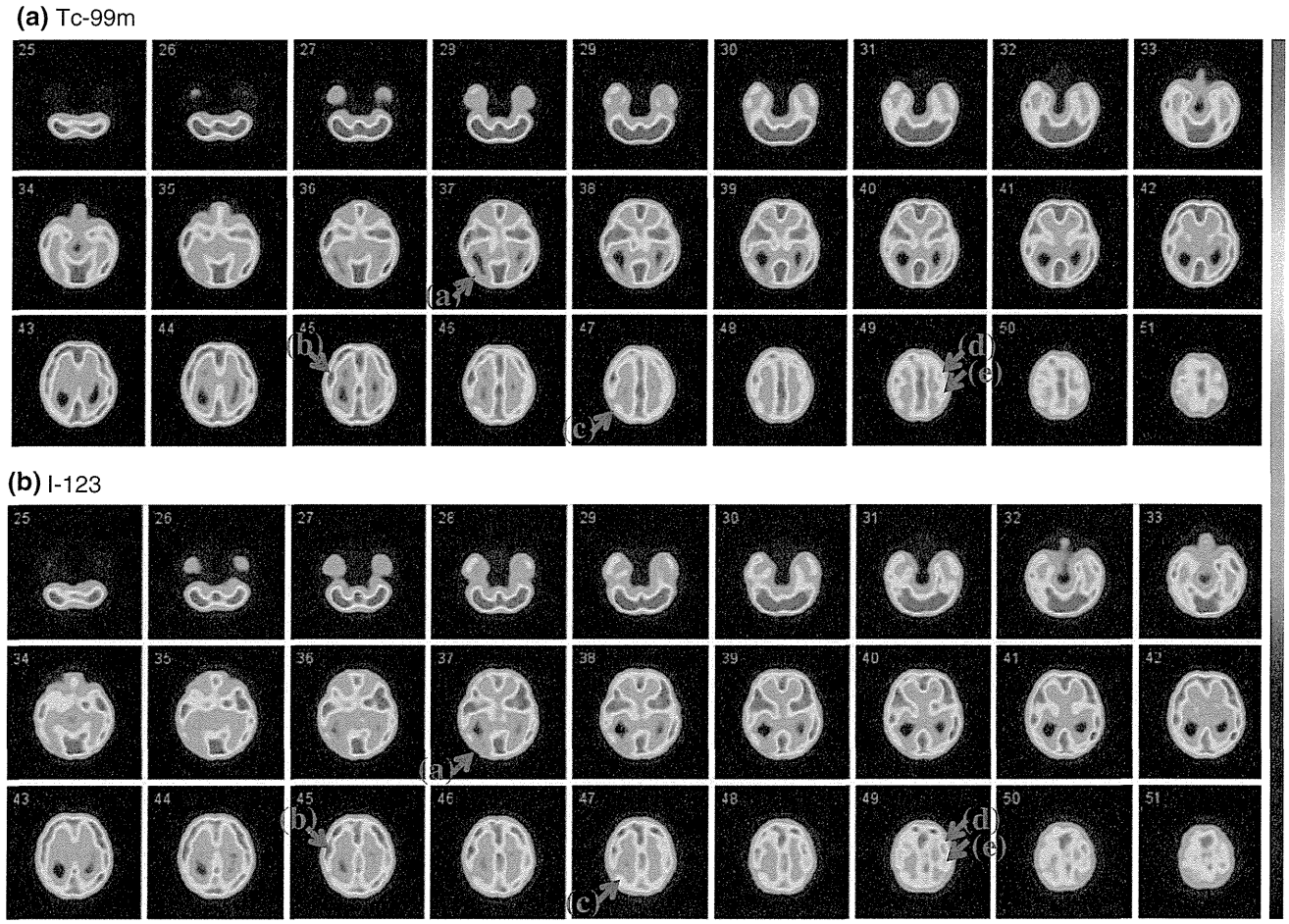

Fig. 5 SPECT images of the phantom filled with a ^{99m}Tc solution (*top*) and ^{123}I solution (*bottom*) in the grey matter compartment and a K_2HPO_4 solution in the bone compartment. Both images are aligned to the digital design shown in Fig. 4. SPECT images of the phantom filled with a ^{99m}Tc solution (*top*) and ^{123}I solution (*bottom*) in the grey matter compartment and a K_2HPO_4 solution in the bone compartment. Both images are aligned to the digital design shown in Fig. 4

This phantom may help evaluating the quality of clinical PET and SPECT brain images assessed with a variety of equipment installed at different institutions. There are several error factors that may cause distortion or irregular radioactivity distribution in the reconstructed images, attributed to imperfect attenuation- or scatter-correction procedures and/or other physical error sources. Quantitatively assessing these factors are often important in multicenter-clinical trials using existing SPECT and PET devices. Recently, Joshi et al. [12] proposed to assess the cross-consistency of PET images from different institutions using the Hoffman 3-dimensional brain phantom. The 3-dimensional brain phantom presented in this article may be better suited for such purpose. Joshi et al. [12] demonstrated that errors introduced by the attenuation and scatter correction procedures are significant and vary depending on the PET device. They also demonstrated that these errors are very different for human brain as compared with those for the Hoffman 3D brain phantom, because of the cylindrical shape of the Hoffman brain phantom with no skull or neck in the Hoffman 3D brain phantom. The phantom developed in this study might be better suited for determination of the attenuation and scatter correction errors for PET in multicentre studies. Further, advantage of the present phantom could be in the usage of evaluating brain SPECT images. Brain SPECT reconstruction often employs a software-based head contour detection for generating an attenuation coefficient distribution, as also done in QSPECT software. The present phantom is suitable in order to evaluate adequacy of the head-contour detection algorithm. Additional error factor could be due to the contribution of radioactivity outside of FOV. This might be evaluated by placing additional radioactivity source that simulates the clinical distribution for each radiotracer. Further systematic studies would be needed in order to confirm the real contribution in multicenter studies using SPECT.

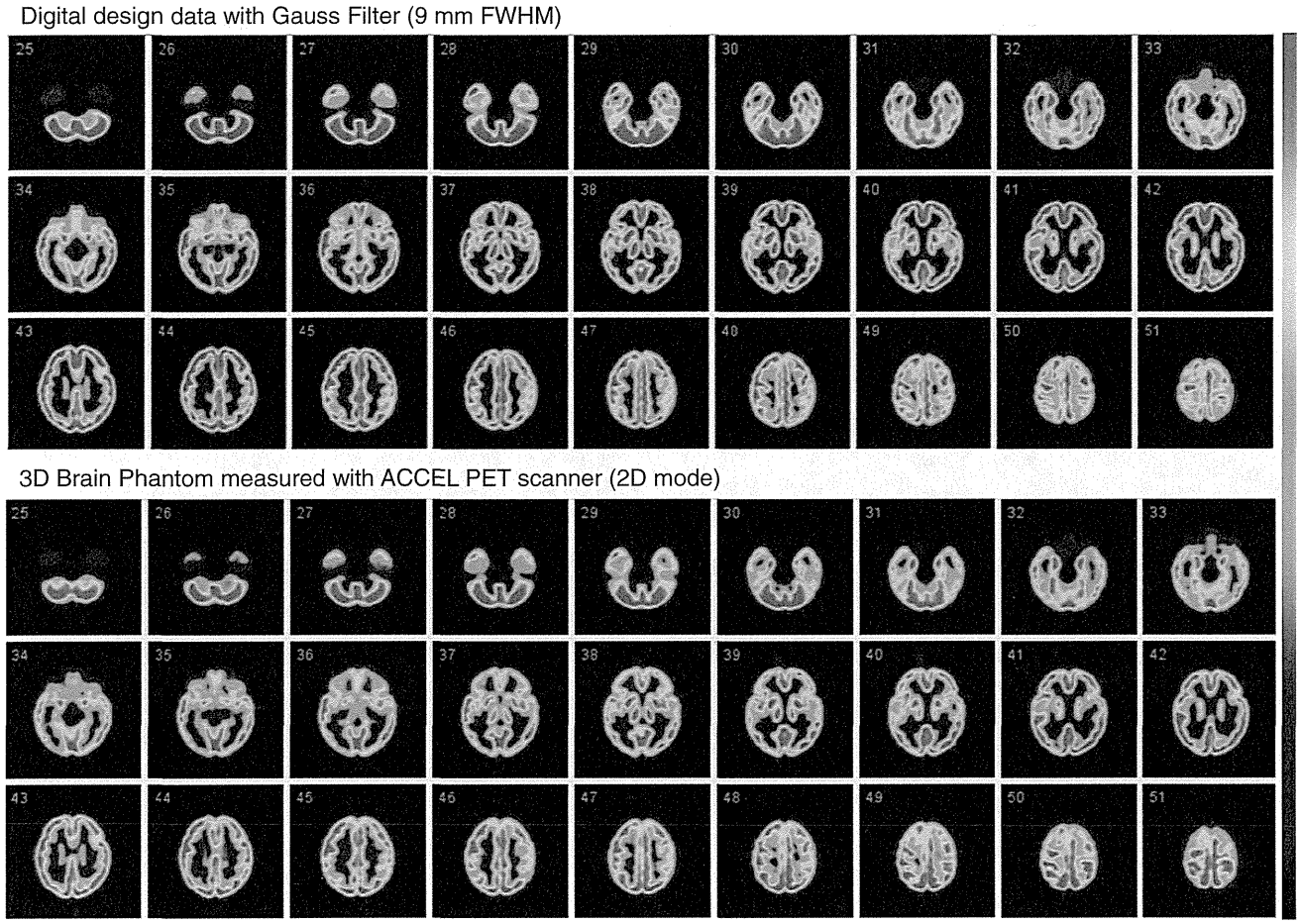

Fig. 6 Digital design of the grey matter area of the phantom after a smoothing operation with a Gaussian Filter of 9-mm full-width at half maximum (*top*), and PET images of the phantom filled with a ^{18}F solution (*bottom*). PET images are aligned to the digital design shown on *top*

The photo-curable polymer has been known to absorb water into the polymer materials and thus could alter the volumes. However, a recently developed water-repellent epoxy-resin (TSR-829) [13] seemed to be an appropriate material for the phantom, as there was minimal dilution of the water-liquid into the resin. The persistence of water in the grey matter and bone compartments after removing the water-liquid is attributed to the surface tension of water. The total weight of the phantom could become the original value when removing the water from the phantom, after 1 day of dry. Although further careful investigations are needed, the results in the present study suggest that this phantom is an adequate tool to evaluate PET/SPECT image quality.

A systematic discrepancy of 11.6 mL (approximately 2 %) was observed in the grey matter volume compared to the digital design. This could have occurred during the axial interpolation in the CAD procedures. Note that the digital data are given as tomographic data at 3.6-mm intervals, and a 3-dimensional interpolation was done to establish the slice-to-slice connectivity. Therefore, the digital data are not necessarily identical to the actual structure of the constructed phantom. However, the difference was not clearly visible in the X-ray CT images compared with the digital design. Intrinsic differences should be present in the precise structure and volume of the constructed phantom, but the reproducibility of the phantom is probably a more important issue. Further investigation is needed.

One drawback of the present 3-dimensional brain phantom compared to the Hoffman 3-dimensional phantom is that there is no structure corresponding to the white matter region. It is theoretically possible to insert small structures in the white matter regions, but additional work will be required to establish a liquid flow in these regions. In addition, air bubbles may be difficult to be removed, requiring further technical challenges.

The reconstruction program used in this study was a QSPECT program and was recently evaluated in a multicenter study [17]. The study demonstrated the adequacy of quantitating cerebral blood flow images both at rest and after acetazolamide treatment in clinical institutions, but

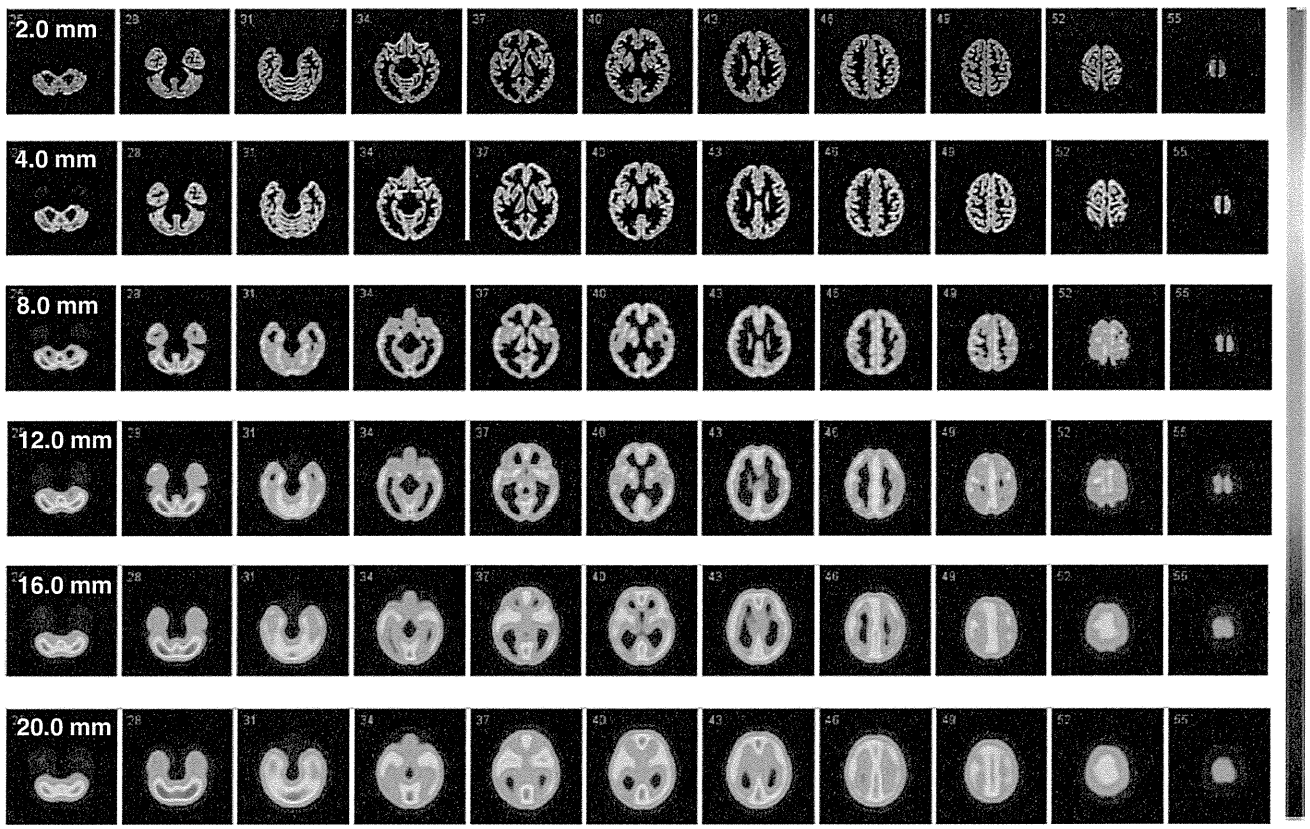

Fig. 7 Digital images of the grey matter region of the phantom with various magnitudes of the 3-dimensional Gaussian filter. The magnitude of the filter is given as full-width at half-maximum. Smoothing reduces the contrast, and the magnitude of modification varies at different regions, depending on the structure

further evaluations of the physical accuracy and cross-institutional consistency of reconstructed images are required among the participating institutions. The present 3-dimensional brain phantom might be valuable for this purpose, particularly when data are obtained with a variety of clinical settings and equipment. These studies are highly desired in the future.

A recent report also suggested the impact of utilizing the SPECT device in multicenter clinical trials. This is based on the physical features of the SPECT equipment, namely that the magnitude of the two major sources of attenuation and scatter errors is independent of the scanner in SPECT, unlike in PET. Scatter and attenuation occur in the object and are thus object dependent, but are not dependent on the geometry of the imaging equipment [18]. Therefore, once a software program is developed to provide accurate image reconstruction with compensation for both attenuation and scatter, the program should be able to provide quantitative images that are intrinsically independent of the geometric design of the SPECT cameras. This is an attractive feature of SPECT for multicenter clinical studies. The present 3-dimensional brain phantom would be valuable in order to verify this concept.

Conclusion

A 3-dimensional brain phantom containing the grey matter, skull, and tracheal structures with a realistic head contour has been developed using a laser-modelling technique with a photo-curable polymer (transparent TSR0829; 1.07 g/mL). The high consistency with digital data and reproducibility across constructions suggest that this phantom can be used for multicenter evaluations of PET and SPECT images.

Acknowledgments The authors would like to thank Ms. Kagari Takada from GK-Design Studio, Suita City, Japan, for help manipulating the 3-dimensional digital data. Thanks are also given to Mr. Shota Murakami from National Cerebral and Cardiovascular Center, Suita City, Japan for assistance with the data and software. The present study was supported by a Grant from the Ministry of Health, Labour and Welfare (MHLW) of Japan, and also partly by the Japan Cardiovascular Research Foundation, Suita City, Japan. No potential conflicts of interest were disclosed.

References

1. Iida H, Nakagawa J, Yamada S, Matsuda H, Maruno H, Nakajima T, et al. Image reconstruction in SPECT: standardization of image processing. Kaku Igaku. 2009;46:109–11.
2. Iida H, Narita Y, Kado H, Kashikura A, Sugawara S, Shoji Y, et al. Effects of scatter and attenuation correction on quantitative assessment of regional cerebral blood flow with SPECT. J Nucl Med. 1998;39:181–9.
3. Kemp BJ, Prato FS, Dean GW, Nicholson RL, Reese L. Correction for attenuation in technetium-99 m-HMPAO SPECT brain imaging. J Nucl Med. 1992;33:1875–80.
4. Kim KM, Varrone A, Watabe H, Shidahara M, Fujita M, Innis RB, et al. Contribution of scatter and attenuation compensation to SPECT images of nonuniformly distributed brain activities. J Nucl Med. 2003;44:512–9.
5. Stodilka RZ, Kemp BJ, Prato FS, Nicholson RL. Importance of bone attenuation in brain SPECT quantification. J Nucl Med. 1998;39:190–7.
6. Bloomfield PM, Spinks TJ, Reed J, Schnorr L, Westrip AM, Livieratos L, et al. The design and implementation of a motion correction scheme for neurological PET. Phys Med Biol. 2003;48:959–78.
7. Ter-Antonyan R, Jaszczak RJ, Greer KL, Bowsher JE, Metzler SD, Coleman RE. Combination of converging collimators for high-sensitivity brain SPECT. J Nucl Med. 2009;50:1548–56.
8. Woo S, Watabe H, Choi Y, Kim K, Park C, Bloomfield M, et al. Sinogram-based motion correction of pet images using optical tracking motion tracking system and list-mode data acquisition. IEEE Trans Nucl Sci. 2004;51:782–8.
9. Ardekani BA, Braun M, Hutton BF, Kanno I, Iida H. Minimum cross-entropy reconstruction of PET images using prior anatomical information. Phys Med Biol. 1996;41:2497–517.
10. Muller-Gartner HW, Links JM, Prince JL, Bryan RN, McVeigh E, Leal JP, et al. Measurement of radiotracer concentration in brain gray matter using positron emission tomography: MRI-based correction for partial volume effects. J Cereb Blood Flow Metab. 1992;12:571–83.
11. Hoffman EJ, Cutler PD, Digby WM. Mazziotta JC 3-D phantom to simulate cerebral blood flow and metabolic images for PET. IEEE Trans Nucl Sci. 1990;37:616–20.
12. Joshi A, Koeppe RA, Fessler JA. Reducing between scanner differences in multi-center PET studies. Neuroimage. 2009;46:154–9.
13. Hagiwara T. Recent progress of polymer materials for laser-modeling. Sokeizai. 2005;46:19–23.
14. de Dreuille O, Strijckmans V, Almeida P, Loc'h C, Bendriem B. Bone equivalent liquid solution to asses accuracy of transmission measurements in SPECT and PET. IEEE Trans Nucl Sci. 1997;44:1186–90.
15. Ichihara T, Motomura N, Ogawa K, Hasegawa H, Hashimoto J, Kubo A. Evaluation of SPET quantification of simultaneous emission and transmission imaging of the brain using a multi-detector SPET system with the TEW scatter compensation method and fan-beam collimation. Eur J Nucl Med. 1996;23:1292–9.
16. Iida H, Eberl S, Kim KM, Tamura Y, Ono Y, Nakazawa M, et al. Absolute quantitation of myocardial blood flow with ^{201}Tl and dynamic SPECT in canine: optimisation and validation of kinetic modelling. Eur J Nucl Med Mol Imaging. 2008;35:896–905.
17. Iida H, Nakagawara J, Hayashida K, Fukushima K, Watabe H, Koshino K, et al. Multicenter evaluation of a standardized protocol for rest and acetazolamide cerebral blood flow assessment using a quantitative SPECT reconstruction program and split-dose 123I-iodoamphetamine. J Nucl Med. 2010;51:1624–31.
18. Graham LS, Fahey FH, Madsen MT, van Aswegen A, Yester MV. Quantitation of SPECT performance: Report of Task Group 4, Nuclear Medicine Committee. Med Phys. 1995;22:401–9.

Nuclear Instruments and Methods in Physics Research A 702 (2013) 111–113

Contents lists available at SciVerse ScienceDirect

Nuclear Instruments and Methods in Physics Research A

journal homepage: www.elsevier.com/locate/nima

Verification of a semi-automated MRI-guided technique for non-invasive determination of the arterial input function in ^{15}O-labeled gaseous PET

Satoshi Iguchi [a], Yuki Hori [a], Tetsuaki Moriguchi [a], Naomi Morita [b], Akihide Yamamoto [a], Kazuhiro Koshino [a], Hidekazu Kawashima [a], Tsutomu Zeniya [a], Jun-ichiro Enmi [a], Hidehiro Iida [a,*]

[a] Department of Investigative Radiology, National Cerebral and Cardiovascular Center Research Institute, 5-7-1, Fujishirodai, Suita, Osaka, 565-8565, Japan
[b] Department of Radiology, National Cerebral and Cardiovascular Center Hospital, 5-7-1, Fujishirodai, Suita, Osaka, 565-8565, Japan

ARTICLE INFO

Available online 25 August 2012

Keywords:
Input function
Spillover correction
Partial volume effect
^{15}O PET

ABSTRACT

A semi-automated MR-guided technique has been evaluated for non-invasive estimation of cerebral metabolic rate of oxygen ($CMRO_2$) using the sequential administration of ^{15}O oxygen (O_2) and ^{15}O carbon dioxide (CO_2) during a single PET scan. Two mathematical models, which assess the arterial input function (AIF) from time-activity curves (TAC) in the internal carotid artery region, were tested, namely one with a simple correction for the recovery coefficient (RC) and another with corrections for RC and spillover from surrounding tissues. RC was determined from MRA and black-blood image. RC was also determined from C^{15}O blood volume images as a reference. RC agreed between MR-based and C^{15}O-PET based methods, suggesting validity of MR-based methods. Area-under-the-curve (AUC) of the early portion of estimated AIF agreed with that of measured AIF in both models. AUC of the delayed phase of estimated AIF was largely overestimated in the first model, but was sufficiently improved by the spillover correction implemented in the second model.

1. Introduction

PET study using ^{15}O gases ($^{15}O_2$, $C^{15}O_2$, $C^{15}O$, and $H_2^{15}O$) provides absolute quantification of cerebral blood flow (CBF), cerebral metabolic rate of oxygen ($CMRO_2$), oxygen extraction fraction (OEF), and cerebral blood volume (CBV). The continuous monitoring of the arterial radioactivity concentration using a small detector is prerequisite, but has been considered non-practical for a clinical use due to its invasiveness and the need for labor intensive work. Recent advances in PET devices enable quantitative assessment of time–activity curves (TAC) in the area of the internal carotid artery (ICA), by which arterial input functions (AIF) may be replaced. However, the small structure of the ICA causes systematic underestimation due to small recovery coefficient (RC) and spillover (SP) from the surrounding tissues [1]. Hybrid MR/PET has a potential providing the PET-derive AIF with accurate and reliable corrections for RC and SP using MR-based anatomical information.

This study was intended to develop a semi-automated technique to derive AIF for a series of ^{15}O-PET scans using MR images. Validity of the technique is tested in the series of PET scans performed on healthy volunteers. The impact of RC and SP corrections has also been evaluated.

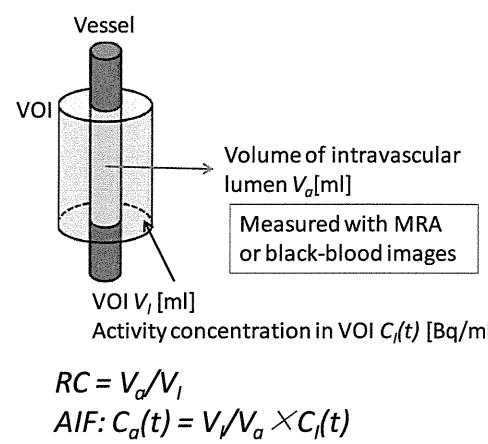

Fig. 1. Mathematical model for AIF estimation with a simple correction for the recovery coefficient (model-1).

Abbreviations: CBF, cerebral blood flow; $CMRO_2$, cerebral metabolic rate of oxygen; OEF, oxygen extraction fraction; CBV, cerebral blood volume; TAC, time-activity curve; ICA, internal carotid artery; AIF, arterial input function; RC, recovery coefficient; SP, spillover; VOI, volume-of-interest; DARG, dual-tracer autoradiographic method; TOF-MRA, time-of-flight magnetic resonance angiography; BB-FRFSE, black-blood fast recovery fast spin echo; AUC, area under the curve

* Corresponding author. Tel.: +81 6 6833 5012x2559; fax: +81 6 6835 5429.
E-mail address: iida@ri.ncvc.go.jp (H. Iida).

0168-9002/$ - see front matter © 2012 Elsevier B.V. All rights reserved.
http://dx.doi.org/10.1016/j.nima.2012.08.037

2. Method

2.1. Imaging protocol

Scans were carried out 9 times, on 7 healthy volunteers of 26+/−10 years old. The scanner was mCT from Siemens enabling 3D PET with adequate corrections for randoms, deadtime count loss, attenuation and scatter. Special attention was made in the scatter correction process to take into account for the strong radioactivity in gaseous form in the facemask. The scan protocol followed a recently proposed rapid dual-tracer autoradiographic method (DARG) [2,3], in which $^{15}O_2$ and $C^{15}O_2$ gases were inhaled sequentially within a 4.5 min interval, during a single PET scan over 9 min. A continuous arterial blood sampling was carried out, and AIF was assessed using a coincidence block detector, with adequate correction for delay and dispersion. Additional PET images were obtained with ^{15}O carbon monoxide (CO) inhalation to measure the RC of a volumes-of-interest (VOI) on ICA. Images were reconstructed at 5 sec interval, to which two VOIs were placed on the ICA region using semi-automated software. MR images were separately acquired on each volunteer with the sequence of 3D time-of-flight MR angiography (TOF-MRA) and 3D black-blood fast recovery fast spin echo (BB-FRFSE). The pixel size of the MR image was $0.6 \times 0.8 \times 1.0$ mm^3 for TOF-MRA and $0.4 \times 0.4 \times 2.0$ mm^3 for BB-FRFSE.

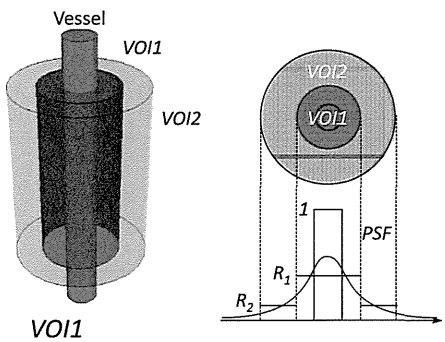

$$VOI1$$
$$C_1(t) = R_1 \times C_a(t) + (1 - R_1) \times C_t(t)$$
$$VOI2$$
$$C_2(t) = R_2 \times C_a(t) + (1 - R_2) \times C_t(t)$$

$C_1(t)$, $C_2(t)$: Activity concentration in VOI 1 and 2
R_1, R_2 : RC in VOI 1 and 2
$C_a(t)$: Radioactivity concentration in arterial blood
$C_t(t)$: Radioactivity concentration in surrounding tissue

Fig. 2. Mathematical model for AIF estimation with recovery coefficient and spillover correction (model-2).

Table 1
Comparison of AUC in the early phase of O_2 and CO_2 inhalation with a simple correction for the recovery coefficient.

	AUC ratio for O_2 (0–60 sec)			AUC ratio for CO_2 (0–60 sec)		
Subject	TOF-MRA	BB-FRFSE	CO	TOF-MRA	BB-FRFSE	CO
001-1	0.88	0.91	0.92	0.89	0.92	0.92
002-1	1.15	1.22	1.21	1.12	1.18	1.21
003-1	1.41	1.14	1.13	1.29	1.05	1.13
004-1	1.06	0.96	1.02	1.13	1.02	1.02
005-1	1.15	1.04	1.03	1.20	1.09	1.03
006-1	1.17	1.11	1.07	1.22	1.16	1.07
006-2	1.32	1.25	1.22	1.33	1.26	1.22
007-1	0.92	0.87	0.95	1.01	0.96	0.95
007-2	1.11	1.05	1.11	0.96	0.91	1.11
Mean	1.13	1.06	1.07	1.13	1.06	1.07
SD	0.17	0.13	0.11	0.15	0.12	0.11

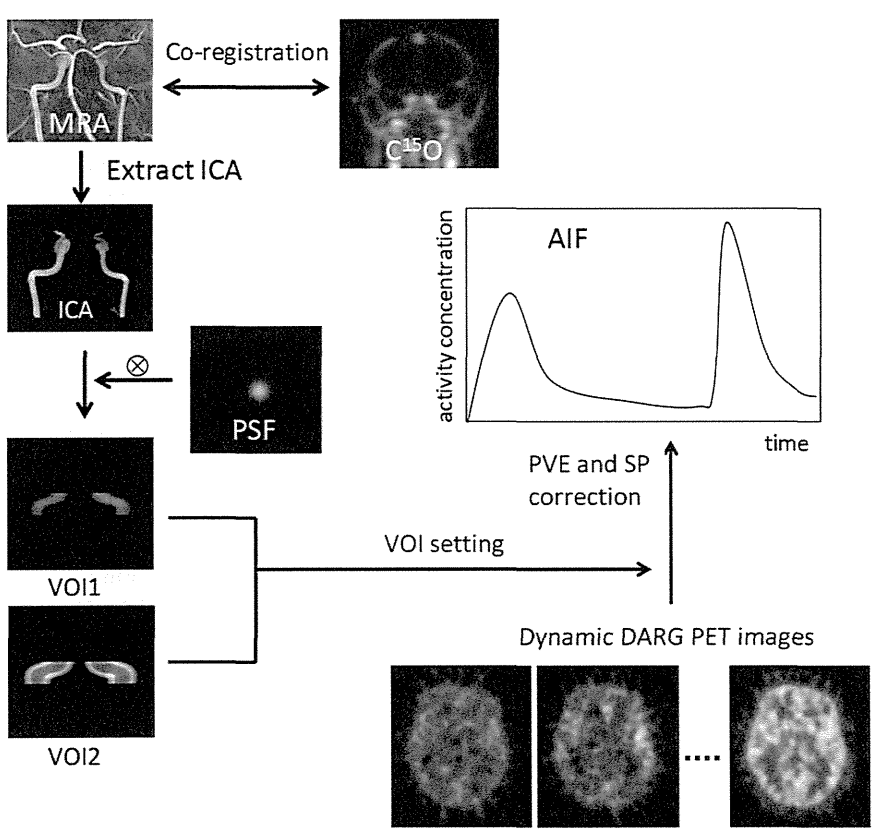

Fig. 3. Image processing for the AIF estimation by using semi-automated software. The process includes co-registration of MRI and PET images, automated extraction of ICA region, and calculation of AIF from dynamic PET images with RC and SP correction using two VOIs.

Table 2
Comparison of AUC in delayed phase of O_2 and CO_2 inhalation with a simple correction for the recovery coefficient.

	AUC ratio for O_2 (60–120 sec)			AUC ratio for CO_2 (60–120 sec)		
Subject	TOF-MRA	BB-FRFSE	CO	TOF-MRA	BB-FRFSE	CO
001-1	1.63	1.69	1.67	2.10	2.18	1.67
002-1	1.65	1.75	1.69	2.58	2.73	1.69
003-1	2.50	2.03	1.95	3.33	2.7	1.95
004-1	1.72	1.56	1.57	2.53	2.29	1.57
005-1	1.67	1.51	1.41	2.12	1.92	1.41
006-1	1.72	1.63	1.47	1.99	1.89	1.47
006-2	1.74	1.65	1.52	1.90	1.8	1.52
007-1	1.40	1.33	1.31	1.66	1.57	1.31
007-2	1.35	1.28	1.29	1.68	1.59	1.29
Mean	1.71	1.60	1.54	2.21	2.07	1.54
SD	0.33	0.22	0.21	0.53	0.43	0.21

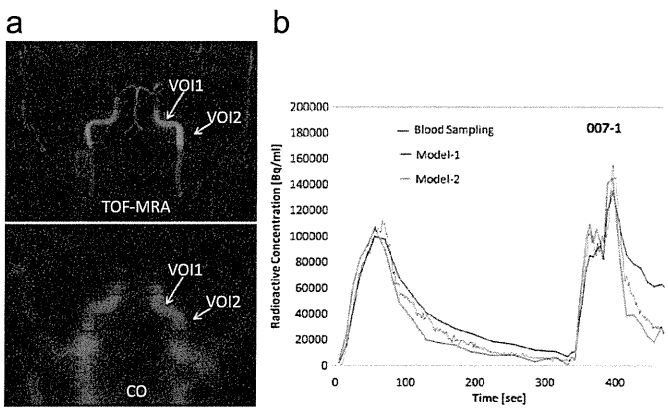

Fig. 4. a: Example of VOI setting fused on maximum projection images of TOF-MRA and CO PET data. VOI 1 and 2 were shown as red and blue region, respectively. b: Measured and estimated input functions in one subject. AIFs were estimated with the mathematical model-1 and model-2.

2.2. Model-1 (only RC correction)

To correct for the underestimation of the input function from ICA TAC, a mathematical model shown in Fig. 1 was applied to determine AIF with a correction for RC. The RC, which was defined as the volume of intravascular lumen-to-the volume of VOI ratio, was calculated using TOF-MRA and BB-FRFSE anatomical images, and was applied to ICA TAC to determine RC-corrected AIFs. RC was also determined from the $C^{15}O$ blood volume image in PET, and was applied to determine AIF.

2.3. Model-2 (RC and SP correction)

Correction for SP of radioactivity from surrounding tissues was taken into account, in addition to the RC correction described in the model-1. The mathematical model shown in Fig. 2 was used, and AIF was determined for given RC values for each of 2 VOIs. The process of image analysis for the AIF estimation using model-2 is shown in Fig. 3.

3. Results

The results of area under the curve (AUC) ratio for the three methods to determine RC for early portion (initial 60 sec) of $^{15}O_2$ and $C^{15}O_2$ scans obtained using the model-1 are summarized in Table 1. Similarly, the results for the delayed portion (60–120 sec) are summarized in Table 2. AIFs determined from ICA were 2.5–4.0 smaller than the measured AIFs. The simple correction for RC using TOF-MRA, BB-FRFSE, and CO images improved the agreement of AUC in the early part, but significantly overestimated in the delayed part.

Table 3
Comparison of AUC in early phase of O_2 and CO_2 inhalation with RC and SP correction.

	AUC ratio for O_2 (0–60 sec)		AUC ratio for CO_2 (0–60 sec)	
Subject	Model-1	Model-2	Model-1	Model-2
001-1	0.94	0.65	1.07	0.84
002-1	1.43	1.25	1.45	1.20
003-1	1.48	0.96	1.46	0.99
004-1	1.18	1.00	1.29	0.91
005-1	1.29	0.89	1.27	0.98
006-1	1.28	1.20	1.32	1.20
006-2	1.44	1.18	1.47	1.21
007-1	1.02	1.04	1.08	1.07
007-2	1.07	1.09	0.93	0.97
Mean	1.24	1.03	1.26	1.04
SD	0.20	0.18	0.20	0.14

Table 4
Comparison of AUC in delayed phase of O_2 and CO_2 inhalation with RC and SP correction.

	AUC ratio for O_2 (60–120 sec)		AUC ratio for CO_2 (60–120 sec)	
Subject	Model-1	Model-2	Model-1	Model-2
001-1	1.46	0.77	2.32	0.81
002-1	1.75	1.20	2.91	1.09
003-1	2.25	1.19	3.69	1.05
004-1	1.59	0.99	2.88	0.73
005-1	1.62	0.84	2.24	0.84
006-1	1.68	1.09	2.27	0.99
006-2	1.66	1.01	2.19	0.80
007-1	1.30	0.89	1.83	0.79
007-2	1.11	0.78	1.56	0.85
Mean	1.60	0.97	2.43	0.88
SD	0.32	0.17	0.64	0.13

Corrections for SP in addition to RC using the two VOIs (Fig. 4a) improved the agreement in AUC as compared with the invasive AIFs particularly for the delayed portion for both O_2 and CO_2 inhalation periods, as shown in Fig. 4b. The results of AUC comparison of model-1 and model-2 were summarized in Tables 3 and 4.

4. Conclusion

In the present study, we demonstrated the non-invasive MRI-guided AIF estimation from TAC in the ICA region in ^{15}O labeled gaseous PET. The AUC of the early phase of estimated AIF well agreed with that of measured AIF. On the other hand, The AUC of the delayed phase of estimated AIF was largely overestimated in model-1, and improved in model-2 by incorporating the SP correction with additional VOI placed surrounding area of the ICA.

These findings suggest that the combination of MR with ^{15}O gaseous PET enables a rapid and quantitative assessment of oxygen utilization simultaneously with the cerebral perfusion, providing unique opportunity for clinical research.

References

[1] P. Zanotti-Fregonara, E.M. Fadaili, R. Maroy, C. Comtat, A. Souloumiac, S. Jan, M.-J. Ribeiro, V. Gaura, A. Bar-Hen, R. Trebossen, Journal of Cerebral Blood Flow and Metabolism 29 (2009) 1825.
[2] N. Kudomi, T. Hayashi, N. Teramoto, H. Watabe, N. Kawachi, Y. Ohta, K.M. Kim, H. Iida, Journal of Cerebral Blood Flow and Metabolism 25 (2005) 1209.
[3] N. Kudomi, H. Watabe, T. Hayashi, H. Iida., Physics in Medicine and Biology 52 (2007) 1893.

J Artif Organs
DOI 10.1007/s10047-012-0676-y

ORIGINAL ARTICLE

Implantation study of small-caliber "biotube" vascular grafts in a rat model

Masashi Yamanami · Hatsue Ishibashi-Ueda · Akihide Yamamoto · Hidehiro Iida · Taiji Watanabe · Keiichi Kanda · Hitoshi Yaku · Yasuhide Nakayama

Received: 7 July 2012 / Accepted: 9 November 2012

Abstract We developed autologous vascular grafts, called "biotubes," by simple and safe in-body tissue architecture technology, which is a practical concept of regenerative medicine, without using special sterile conditions or complicated in vitro cell treatment processes. In this study, biotubes of extremely small caliber were first auto-implanted to rat abdominal aortas. Biotubes were prepared by placing silicone rods (outer diameter 1.5 mm, length 30 mm) used as a mold into dorsal subcutaneous pouches in rats for 4 weeks. After argatroban coating, the obtained biotubes were auto-implanted to abdominal aortas ($n = 6$) by end-to-end anastomosis using a custom-designed sutureless vascular connecting system under microscopic guidance. Graft status was evaluated by contrast-free time-of-flight magnetic resonance angiography (TOF-MRA). All grafts were harvested at 12 weeks after implantation. The patency rate was 66.7 % (4/6). MRA showed little stenosis and no aneurysmal dilation in all biotubes. The original biotube had wall thickness of about 56.2 ± 26.5 μm at the middle portion and mainly random and sparse collagen fibers and fibroblasts. After implantation, the wall thickness was 235.8 ± 24.8 μm. In addition, native-like vascular structure was regenerated, which included (1) a completely endothelialized luminal surface, (2) a mesh-like elastin fiber network, and (3) regular circumferential orientation of collagen fibers and α-SMA positive cells. Biotubes could be used as small-caliber vascular prostheses that greatly facilitate the healing process and exhibit excellent biocompatibility in vascular regenerative medicine.

Keywords Biotube · Vascular grafts · Autologous tissue · In vivo tissue engineering · Connective tissue

M. Yamanami (✉) · T. Watanabe · Y. Nakayama (✉)
Division of Medical Engineering and Materials, National Cerebral and Cardiovascular Center Research Institute, 5-7-1 Fujishiro-dai, Suita, Osaka 565-8565, Japan
e-mail: yamanami@koto.kpu-m.ac.jp

Y. Nakayama
e-mail: nakayama.yasuhide.ri@mail.ncvc.go.jp

M. Yamanami · T. Watanabe · K. Kanda · H. Yaku
Department of Cardiovascular Surgery, Kyoto Prefectural University of Medicine, Kyoto, Japan

H. Ishibashi-Ueda
Department of Pathology, National Cerebral and Cardiovascular Center, Osaka, Japan

A. Yamamoto · H. Iida
Department of Biomedical Imaging, National Cerebral and Cardiovascular Center Research Institute, Osaka, Japan

A. Yamamoto · H. Iida
Department of Medical Physics and Engineering, Division of Health Sciences, Graduate School of Medicine, Osaka University, Osaka, Japan

Introduction

Small-caliber arterial substitutes are needed for cardiac and peripheral revascularization procedures. For such small artery bypass grafting procedures, autologous arterial (e.g., internal thoracic artery and radial artery) or venous (e.g., saphenous vein) grafts are still the ideal vascular substitute [1–3]. However, many patients do not have a vessel suitable for use owing to the poor quality, inadequate size or length, or previous harvesting of such vessels [4]. Moreover, a second surgical procedure is required in order to obtain the necessary vessel initially. Small-caliber arterial substitutes have generally proved

Published online: 29 November 2012

inadequate largely because of the formation of thromboses and intimal hyperplasia [5, 6].

We developed autologous prosthetic tissues using "in-body tissue architecture" technology, which is a novel and practical approach of regenerative medicine based on the tissue-encapsulation phenomenon of foreign materials in living bodies [7]. This technology has the following advantages. The tissue prostheses can be fabricated in a wide range of shapes and sizes to suit the need of individual recipients, and most importantly, these prostheses do not require complex in vitro cell management procedures or exceptionally clean laboratory facilities, which are expensive and time consuming. This technology has been used for the development of cardiovascular tissues such as vascular grafts, namely biotubes [7–11], or heart valves, namely biovalves [12, 13]. Previously, the biotubes with 3-mm diameter were implanted into rabbit carotid arteries [10]. A high patency rate (9/11) was obtained at 12 weeks with endothelialization, dense collagen fibers with regular circumferential orientation, and a few elastin fibers. No aneurysm formation, rupturing, or stenosis was observed for up to 26 months without significant neointimal thickening [11].

In this study, further small-caliber biotubes with an inner diameter of 1.5 mm were auto-implanted to rat abdominal aortas for 12 weeks, and histological changes of biotubes after implantation were evaluated.

Materials and methods

Preparation of biotubes

A total of six adult female Wistar rats (age 8 weeks, weight 238.8 ± 58.6 g) were used in this experiment. All animals received care according to the Principles of Laboratory Animal Care (formulated by the National Institutes of Health, publication no.56-23, received 1985), and the research protocol (no. 9044) was approved by the ethics committee of the National Cerebral and Cardiovascular Center.

A silicone rod (diameter, 1.5 mm; length, 30 mm; Tigers Polymer, Osaka, Japan) was used as a mold. The rats were anesthetized with 1.5 % isoflurane (v/v air). A small incision was made in the shaved dorsal skin, and three molds were placed in dorsal subcutaneous pouches of each animal. After 4 weeks, the rats were anesthetized with 1.5 % isoflurane, and the implants were harvested. The three biotubes (internal diameter 1.5 mm) per one rat were obtained from the implants after trimming the peripheral tissues and pulling out the rods. One of the biotubes was used for autologous transplantation, and the others were used for measurement of burst strength or histological evaluation.

Measurement of burst strength

Biotubes ($n = 6$) and native abdominal aortas ($n = 6$) were used as samples. The native abdominal aortas were obtained at sacrificing for the implanted biotubes. One end of the biotubes was closed by tying with 4-0 silk threads and held at fixed distance to restrict the longitudinal distension and elongation. To the other end, a stainless-steel tube of 1.5 mm in external diameter was fixed with 4-0 silk threads to act as a cannula. Saline solution was pumped into the luminal cavities of the biotubes through the stainless steel tube at a rate of 50 mmHg/s until the biotubes ruptured. The burst strength was denoted by the water pressure at the instant of tube rupture, as measured by a pressure transducer (N5901; Nihon Denki Sanei, Inc., Tokyo, Japan).

Implantation of biotubes

Biotubes (length 20 mm; $n = 6$) were implanted to the infrarenal abdominal aorta using "the sutureless vascular connecting system" under microscopic guidance, similar to our previously reported system [14]. The connecting system consists of an introducing sheath and a connecting device. The introducing sheath was prepared by remodeling the catheter tubing (polyurethane of the 16G BD Insyte^{TM}, Becton, Dickinson and Company, NJ, USA). The connecting devices were custom-designed from the catheter (polyurethane, 16G BD Insyte^{TM}, Becton, Dickinson and Co., Franklin Lakes, NJ, USA). The dimensions of the devices were: 1.5 mm in length, 1.7 mm in external diameter, and 1.3 mm in internal diameter. In the wall of the catheter, circular micropores were processed by a CAD-assisted YAG laser ablation technique. Pore diameter was 400 μm, pore-to-pore distance was 500 μm, and the pore area to the entire area was 60 %.

Biotubes were treated by coating with argatroban (1 mg/cm^2; Mitsubishi Chemical Co., Tokyo, Japan) for 10 min in order to make it antithrombogenic immediately before implantation. The connecting devices were inserted into the proximal and distal ends of the rat aorta through the introducing sheath. Subsequently, the treated aortic ends were inserted into biotubes, followed by banding from the outside of the biotubes with 7-0 silk threads (Alfresa, Osaka, Japan). Patency was examined at the time of surgery by direct inspection. The wound was closed with 4-0 nylon sutures. Thereafter, the rats had free access to standard food and water. No anticoagulants or antiplatelet agents were administered postoperatively. After 12 weeks of implantation all biotubes were harvested.

Evaluation of graft status

Graft status was evaluated at 6 and 12 weeks after transplantation by 3-T contrast-free time-of-flight magnetic resonance angiography (TOF-MRA) under anesthesia induced by an intramuscular injection of pentobarbital (40 mg/kg). A human whole-body 3-T magnetic resonance imaging (MRI) scanner (Sigma, GE Healthcare, Milwaukee, WI, USA) was employed. The gradient coil system was capable of providing a maximum gradient amplitude of 40 mT/m. All sequence programs employed in this study were designed for clinical studies. A developed single-turn surface coil of 62 mm diameter was used for MR imaging. Contrast-free TOF-MRA was performed using a three-dimensional flow-compensated fast spoiled gradient recalled (3D-FSPGR) sequence [repetition time (TR) = 21 ms, echo time (TE) = 5.4 ms (out of phase), flip angle (FA) = 15°, slice thickness = 0.4 mm, field of view (FOV) = 80 mm × 60 mm, matrix = 288 × 192, locs per slab = 128, the number of excitations (NEX) = 1, scanning time = 5 min 58 s]. For suppressing venous signals, a region of 40 mm thickness on the caudal side of the measured slab was saturated. MR angiograms were analyzed by generating the partial maximum intensity projection (pMIP) with a commercial software package (AZE, Tokyo, Japan).

Histological examination

The specimens of the implanted biotubes were fixed with 10 % formalin, embedded in paraffin, sliced into short axis cross sections, and finally stained with hematoxylin-eosin, Masson's trichrome, Elastica van Gieson, or Siriusu red. Immunohistochemistry was performed using monoclonal antibodies against α-smooth muscle actin (anti-human α-SMA mouse monoclonal antibody clone 1A4; Dako Japan, Kyoto, Japan; 1:100 dilution) and factor VIII (anti-human von Willebrand factor mouse monoclonal antibody clone F8/86; Dako Japan, Kyoto, Japan; 1:100 dilution).

Results

Preparation of biotubes

After the molds (Fig. 1a) were inserted into the dorsal subcutaneous pouches of rats for 4 weeks, all molds were completely encapsulated with very thin homogeneous autologous connective tissues (Fig. 1b). Biotubes were obtained by removing the molds from capsule tissues (Fig. 1c). The efficiency of the biotube preparation was 100 %. The burst pressure of biotubes was 1085 ± 525 mmHg (mean ± SD), which is approximately half of that of rat aorta (2478 ± 628 mmHg).

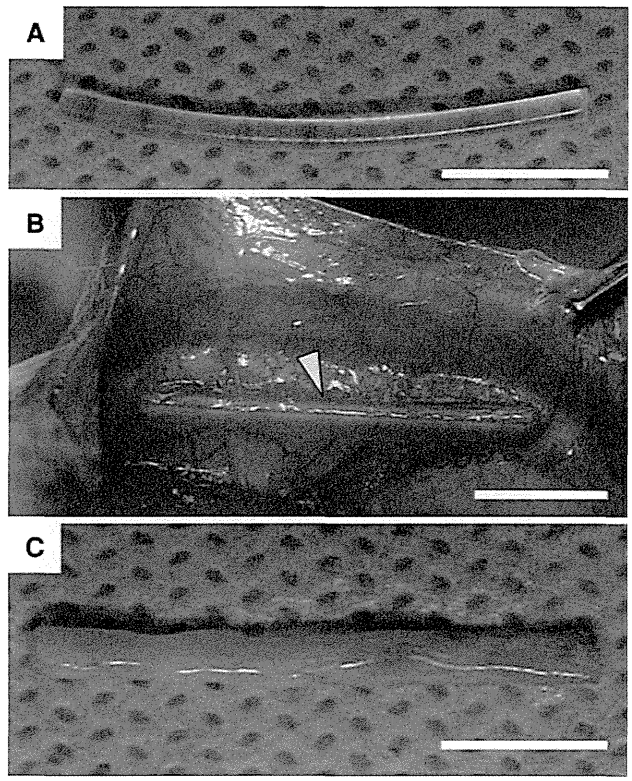

Fig. 1 **a** Silicone rods (diameter 1.5 mm, length 15 mm) were used as the molds. **b** The molds were embedded into dorsal subcutaneous pouches of rats for 4 weeks. The molds were completely encapsulated with connective tissues. **c** The obtained biotubes with thin wall (thickness 56.2 ± 26.5 μm). *Scale bar* 1.0 mm

Biotube implantation

Biotubes could be implanted easily into the rats using a custom-designed sutureless vascular connecting system, where no suturing treatment for anastomosis was needed (Fig. 2a). Total ischemia time for implantation was very short (34.8 ± 12.1 min). No bleeding was observed after declamping (Fig. 2b).

MRA distinctly visualized the patent graft connected to the abdominal aorta together with renal arteries and common iliac arteries (Fig. 3). However, pseudostenosis by artifact of the connection was observed in both anastomosis regions (arrows in Fig. 3). In the midgraft region, little stenosis and no aneurysmal dilation were observed in all patent grafts. The overall patency rate was 66.7 % (4/6). Two of the six grafts were occluded by thrombosis at 6 weeks after implantation.

Implanted biotubes were easily harvested with no damage because there were few adhesions between biotubes and surrounding tissues (Fig. 2c). In the obtained biotubes 12 weeks after implantation, macroscopic observation revealed an extremely flat surface including the region of connecting device, which was completely

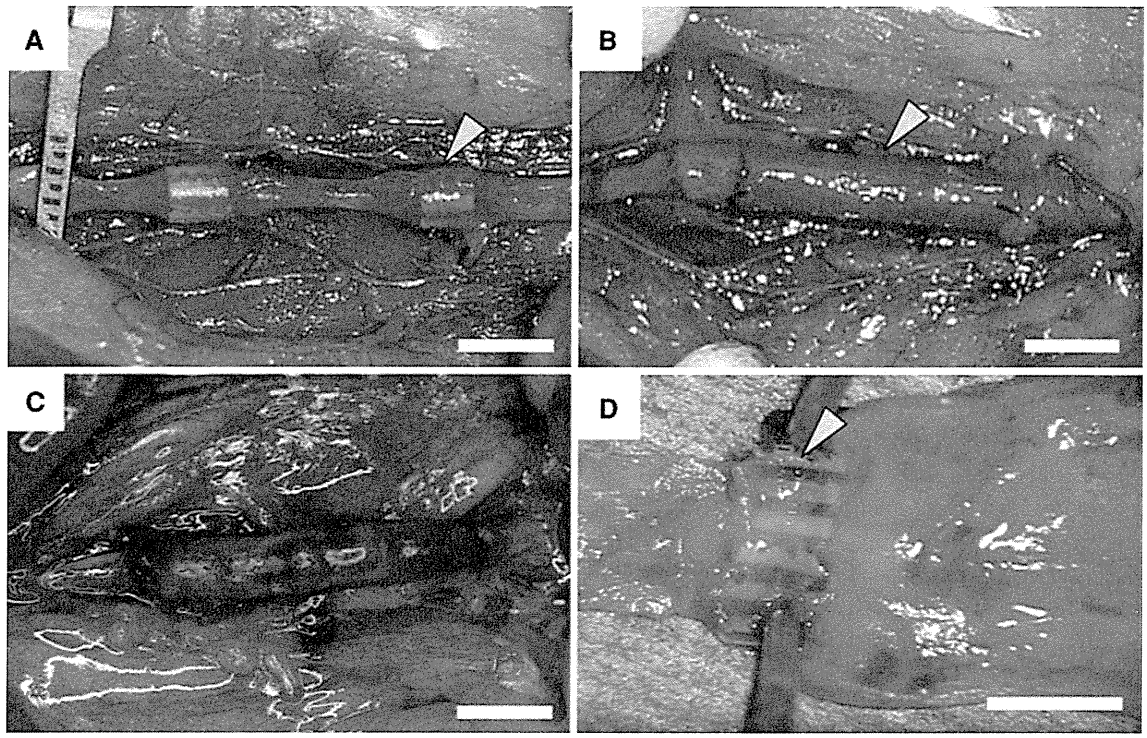

Fig. 2 **a** Insertion of two connecting devices, fabricated from catheter tubing (polyurethane of the 16G BD InsyteTM, Becton, Dickinson and Company, Franklin Lakes, NJ, USA), into the proximal and distal ends of the rat abdominal aorta through the introducing sheath under clamping. **b** The treated aortic ends were inserted into the biotube vascular graft, followed by banding from the outside of the biotube with 7-0 silk threads. Pulsation of the biotubes was noted immediately after declamping. **c** After 12 weeks of implantation, the biotube had little adhesion with surrounding tissues. **d** Macroscopic observation revealed an extremely flat luminal surface including the luminal regions of the connecting devices, which were completely impregnated into the vascular tissues (*scale bar* 3 mm)

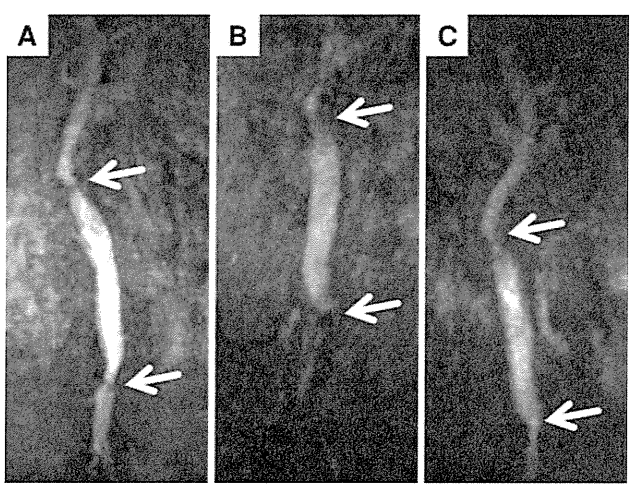

Fig. 3 MRA images of the rat abdominal aorta at 1 (**a**), 6 (**b**) and 12 (**c**) weeks after implantation of biotubes. Upper side of all photos indicates the proximal side. *White arrows* indicate the proximal and distal anastomosis regions of the abdominal aorta. A mechanical stenotic lesion, which may have been due to the anastomosis, was observed in both anastomosis regions. In the midgraft region, neither significant stenosis nor aneurysmal dilation was observed

impregnated into the developed thin tissues (Fig. 2d). In the circumferential cross section of midgraft region, the wall had grown thick, keeping the area of the lumen. Before implantation, wall thickness of the biotubes was 56.2 ± 26.5 μm (Fig. 4a-1). At 12 weeks after implantation, neointima was formed with wall thickness of 235.8 ± 24.8 μm (Fig. 4b-1).

Histological change

Before implantation biotubes were composed of collagen-rich tissue with no elastic fibers (Fig. 4a-2, a-3) and collagen fibers were randomly attached (Fig. 4a-6). No abnormal collection or infiltration of inflammatory cells was observed. The main cell component was fibroblasts with no vascular constituent tissues (Fig. 4a-4, a-5).

On the other hand, after 12 weeks of implantation the neointima was segregated in two layers, where the luminal layer with a mesh-like elastin fiber network (Fig. 4b-3) and circumferential oriented collagen fiber (Fig. 4b-2, b-6) were formed on the almost cell-free dense collagen basement

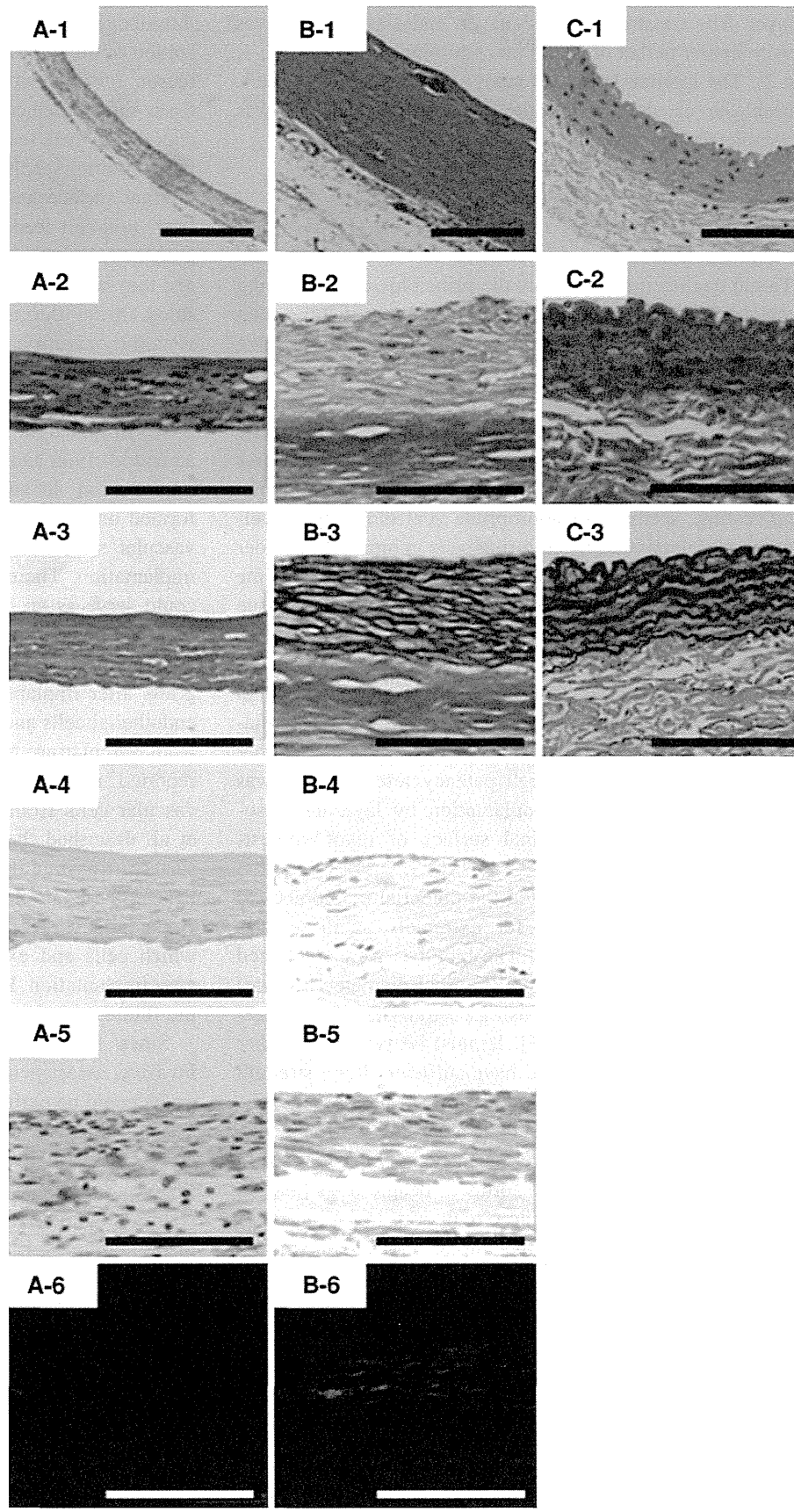

Fig. 4 The circumferential cross section of the biotube before implantation (**a-1–6**) and obtained at 12 weeks after implantation (**b-1–6**). The circumferential cross section of native rat abdominal aorta (**c-1–3**). Stained with H&E (**a-1**, **b-1**, **c-1**), Masson trichrome (**a-2**, **b-2**, **c-2**), Elastica van Giesson (**a-3**, **b-3**, **c-3**), factor VIII (**a-4**, **b-4**), α-SMA (**a-5**, **b-5**), and Sirius red (**a-6**, **b-6**). Masson trichrome stain revealed that it was composed of collagen-rich tissue. Polarizing microscopic observation after Sirius red stain showed circumferential orientation of the collagen fiber after implantation (**b-6**). Elastica van Giesson staining revealed an elastic fiber network in the neointima of the biotube after implantation (**b-3**). Immunohistological staining for factor VIII and α-smooth muscle actin revealed α-smooth muscle actin-positive cells (**b-5**) and endothelial lining at the luminal surfaces (**b-4**) of biotube after implantation (*scale bar* 100 μm)

layer. The construction of collagen and elastin fibers was very similar to that of native rat abdominal aorta (Fig. 4c-1, c-2). The luminal layer had many α-SMA-positive, myofibroblasts or smooth muscle cells (Fig. 4b-5) and was completely covered with endothelial cells (Fig. 4b-4).

Discussion

Tissue engineering combines the principles of engineering and biological sciences to develop viable structures that can replace diseased deficient natural structures. Some investigators have successfully implanted in vitro tissue-engineered vascular grafts in animals by using either decellularized natural tissues or biodegradable synthetic polymers as scaffolds [15–18]. However, these procedures require complicated cell-management protocols, including harvesting, seeding on appropriate scaffolds, and development of neotissues by culturing cells in bioreactors under strictly sterile conditions; all of these procedures are time consuming and expensive. On the other hand, in vivo tissue engineering can produce completely autologous tissues without any artificial support materials. Campbell et al. developed autologous vascular grafts in the abdominal cavities of rats or rabbits. Although the grafts had a relatively large internal diameter (3 mm) for small-caliber native aorta of rats, the high patency rate of 67 % was reported at 4 months of implantation by layering mesothelium cells on the luminal surface of myofibroblast-walled tubes [19].

In this study, we evaluated the potential of biotubes to generate a vascular graft for extremely small arteries (internal diameter 1.5 mm). The biotubes were implanted to the abdominal aorta of rats (internal diameter 1.3 mm) by end-to-end anastomosis using custom-designed sutureless connecting devices [15]. It must be verified whether biotubes can be sutured and have sufficient burst strength to withstand physiologic blood pressure or not. Because the biotubes have adequate mechanical properties for a vascular prosthesis, they were recently applied to carotid arteries [20] and abdominal aortas of beagle dogs [21]. In all implantations for systemic circulation, including those described in this study, neither rupture nor aneurysm formation was observed.

The patency rate of the biotubes at 12 weeks after implantation was high in this study (66.7 %). Because the main components of the original biotubes were collagen fibers and fibroblasts, it was considered that acellular luminal surfaces without endothelial cell coverage carry a substantial risk for thrombosis when exposed to the blood directly. In our previous implantation study of biotubes, all grafts without anti-thrombogenic coating were completely occluded at 2 weeks after implantation [10]. Strong anti-thrombogenicity, provided by the complete endothelialization of the luminal surfaces, is highly desirable. For this reason, most recent studies have focused on the creation of tissue-engineered cardiovascular implants using autologous endothelial cell seeding and bioreactor culturing prior to implantation. Seeding with autologous vascular cells on the luminal surface has provided a much higher patency rate than non-cell-seeded grafts [22]. However, such cell management and processing are complicated and invasive, and they will render the implants prone to infection. In this study, acute thrombus formation was considerably prevented by argatroban coating.

At 12 weeks after implantation, almost complete vascular tissue was re-constructed. Endothelial cells and SMCs migrated into the biotube and became organized into an endothelium and a media-like smooth muscle layer after implantation. In addition, mesh-like elastin network was formed on the basement dense collagen layer. Native-like vascular structure was regenerated in a short period of implantation. Therefore, the autologous connective tissue could serve as an ideal scaffold for vascular wall formation. Some investigators have discussed which cells and extracellular matrix remodeled tissue-engineered vascular grafts after implantation. Kuwabara et al. [23] suspected endothelial cells and smooth muscle cells were regenerated from circulating blood stem cells. Hibino et al. [24] reported neovessel formation arises from ingrowth of vascular cells from the neighboring blood vessel. Erman et al. described that endothelial coverage of the luminal surface, transmural cellular infiltration, and formation of neocapillaries in the graft body are the major graft healing characteristics [17]. In this study, it still remains unclear which cells and extracellular matrix remodeled biotubes after implantation. It is necessary to investigate this issue in the future.

Since the observation by MRA is simple and non-invasive, assessment of the status of small-caliber vascular grafts could be performed in the same rat at different times. The repeatable MRA observation in a single rat enabled correct assessment of the graft status over the follow-up period. Such repeatability will reduce the variation in results stemming from individual differences in experimental animals [25]. By using the connecting system, aortic clump time was only 30 min, which is about half that in the traditional suturing method [14]. Since no bleeding at the connecting parts occurred, hemostasis was very easy in all implantations. In addition, although pseudostenosis by artifacts of the connecting devices was observed at both anastomosis regions, there was no actual stenosis. The stenosis by suturing could lead to serious occlusion in small-caliber grafts. The control of the bleeding and minimal anastomotic stenosis using the connecting system induced reproductive results in the implantation study

independent of the technique of surgeons. On the other hand, there is one notable limitation to this system in that the connecting device was directly exposed to blood flow, which might promote thrombus formation at the luminal surface of the device. Because of the small caliber of the grafts, even small thrombi could result in occlusion. However, the early endothelialization promoted by the microporous mesh structure could prevent this complication. Therefore, this system minimizing the blood flow interruption to obtain complete and reliable anastomosis was appropriate for this study.

Conclusion

The biotube vascular grafts provided high patency even when implanted in extremely small-caliber vessels with internal diameter of 1.5 mm. An almost complete artery-like structure with cellular components of endothelial cells and smooth muscle cells and extracellular components of collagen and elastin was formed only 12 weeks after implantation. Biotubes could thus be used as small-caliber vascular prostheses that greatly facilitated the healing process and exhibited excellent biocompatibility.

Acknowledgments The authors thank Ms. Manami Sone for her technical support in this study. This study was funded in part by a Grant-in-Aid for Scientific Research (B23360374) from the Ministry of Education, Culture, Sports, Science and Technology of Japan.

References

1. Tomizawa Y. Vascular protheses for aortocoronary bypass grafting: a review. Artif Organs. 1995;19:39–45.
2. Ferrari ER, von Segesser LK. Arterial grafting for myocardial revascularization: how better is it? Curr Opin Cardiol. 2006;21(6):584–8.
3. Faries PL, LoGerfo FW, Arora S, Hook S, Pulling MC, Akbari CM, Campbell DR, Pomposelli FB Jr. A comparative study of alternative conduits for lower extremity revascularization: all-autogenous conduit versus prosthetic grafts. J Vasc Surg. 2000;32:1080–90.
4. Daenens K, Schepers S, Fourneau I, Hounthoofd S, Nevelsteen A. Heparin-bonded ePTFE grafts compared with vein grafts in femoropopliteal and femorocrural bypass: 1- and 2-year results. J Vasc Surg. 2009;49:1210–6.
5. Ao PY, Hawthorne WJ, Vicaretti M, Fletcher JP. Development of intimal hyperplasia in six different vascular prostheses. Eur J Vasc Endovascu Surg. 2000;20:241–9.
6. Isenberg BC, Williams C, Tranquillo RT. Small-diameter artificial arteries engineered in vitro. Circ Res. 2006;98(1):25–35.
7. Nakayama Y, Ishibashi-Ueda H, Takamizawa K. In vivo tissue-engineered small-caliber arterial graft prosthesis consisting of autologous tissue (biotube). Cell Transpl. 2004;13:439–49.
8. Watanabe T, Kanda K, Ishibashi-Ueda H, Yaku H, Nakayama Y. Development of biotube vascular grafts incorporating cuffs for easy implantation. J Artif Organs. 2007;10:10–5.
9. Sakai O, Kanda K, Ishibashi-Ueda H, Takamizawa K, Ametani A, Yaku H, Nakayama Y. Development of the wing-attached rod for acceleration of "Biotube" vascular grafts fabrication in vivo. J Biomed Mater Res B Appl Biomater. 2007;83:240–7.
10. Watanabe T, Kanda K, Ishibashi-Ueda H, Yaku H, Nakayama Y. Autologous small-caliber "Biotube" vascular grafts with argatroban loading: a histomorphological examination after implantation to rabbits. J Biomed Mater Res B Appl Biomater. 2010;92:236–42.
11. Watanabe T, Kanda K, Yamanami M, Ishibashi-Ueda H, Yaku H, Nakayama Y. Long-term animal implantation study of biotube—autologous small-caliber vascular graft fabricated by in-body tissue architecture. J Biomed Mater Res B Appl Biomater. 2011;98(1):120–6.
12. Hayashida K, Kanda K, Yaku H, Ando J, Nakayama Y. Development of an in vivo tissue-engineered, autologous heart valve (the biovalve): preparation of a prototype model. J Thorac Cardiovasc Surg. 2007;134:152–9.
13. Yamanami M, Yahata Y, Uechi M, Fujiwara M, Ishibashi-Ueda H, Kanda K, Watanabe T, Tajikawa T, Ohba K, Yaku H, Nakayama Y. Development of a completely autologous valved conduit with the sinus of Valsalva using in-body tissue architecture technology: a pilot study in pulmonary valve replacement in a beagle model. Circulation. 2010;122:S100–6.
14. Sakai O, Nakayama Y, Nemoto Y, Okamoto Y, Watanabe T, Kanda K, Yaku H. Development of sutureless vascular connecting system for easy implantation of small-caliber artificial grafts. J Artif Organs. 2005;8:119–24.
15. Lopez-Soler RI, Brennan MP, Goyal A, Wang Y, Fong P, Tellides G, Sinusas A, Dardik A, Breuer C. Development of a mouse model for evaluation of small diameter vascular grafts. J Surg Res. 2007;139:1–6.
16. Narita Y, Kagami H, Matsunuma H, Murase Y, Ueda M, Ueda Y. Decellularized ureter for tissue-engineered small-caliber vascular graft. J Artif Organs. 2008;11:91–9.
17. Pektok E, Nottelet B, Tille JC, Gurny R, Kalangos A, Moeller M, Walpoth BH. Degradation and healing characteristics of small-diameter poly(epsilon-caprolactone) vascular grafts in the rat systemic arterial circulation. Circulation. 2008;118:2563–70.
18. Shin'oka T, Imai Y, Ikada Y. Transplantation of a tissue-engineered pulmonary artery. N Engl J Med. 2001;15:532–3.
19. Campbell JH, Efendy JE, Campbell GR. Novel vascular graft grown within recipient's own peritoneal cavity. Circ Res. 1999;85:1173–8.
20. Watanabe T, Kanda K, Yamanami M, Yaku H, Nakayama Y. Biotubes designed for large animals: auto-implantation to the carotid artery of the beagle dogs. Int J Artif Organs. 2008;31:601.
21. Watanabe T, Yamanami M, Kanda K, Ishibashi-Ueda H, Yaku H, Nakayama Y. Application of biotube vascular grafts to abcominal region in a beagle model. Int J Artif Organs. 2010;33:466.
22. Shindo S, Takagi A, Whittemore AD. Improved patency of collagen-impregnated grafts after in vitro autogenenous endothelial cell seeding. J Vasc Surg. 1987;6:325–32.
23. Kuwabara F, Narita Y, Yamawaki-Ogata A, Kanie K, Kato R, Satake M, Kaneko H, Oshima H, Usui A, Ueda Y. Novel small-caliber vascular grafts with trimeric Peptide for acceleration of endothelialization. Ann Thorac Surg. 2012;93(1):156–63.
24. Hibino N, Villalona G, Pietris N, Duncan DR, Schoffner A, Roh JD, Yi T, Dobrucki LW, Mejias D, Sawh-Martinez R, Harrington JK, Sinusas A, Krause DS, Kyriakides T, Saltzman WM, Pober JS, Shin'oka T, Breuer CK. Tissue-engineered vascular grafts form neovessels that arise from regeneration of the adjacent blood vessel. FASEB J. 2011;25(8):2731–9.
25. Yamanami M, Yamamoto A, Iida H, Watanabe T, Kanda K, Yaku H, Nakayama Y. 3-Tesla magnetic resonance angiographic assessment of a tissue-engineered small-caliber vascular graft implanted in a rat. J Biomed Mater Res B Appl Biomater. 2010;92:156–60.

Journal of Magnetic Resonance 229 (2013) 101–115

Contents lists available at SciVerse ScienceDirect

Journal of Magnetic Resonance

journal homepage: www.elsevier.com/locate/jmr

Advances in multimodal neuroimaging: Hybrid MR–PET and MR–PET–EEG at 3 T and 9.4 T

N. Jon Shah [a,b,*], Ana-Maria Oros-Peusquens [a], Jorge Arrubla [a], Ke Zhang [a], Tracy Warbrick [a], Jörg Mauler [a], Kaveh Vahedipour [a], Sandro Romanzetti [a], Jörg Felder [a], Avdo Celik [a], Elena Rota-Kops [a], Hidehiro Iida [d], Karl-Josef Langen [a], Hans Herzog [a], Irene Neuner [a,c]

[a] Institute of Neuroscience and Medicine-4, Research Centre Jülich, 52425 Jülich, Germany
[b] Department of Neurology, Faculty of Medicine, JARA, RWTH Aachen University, Aachen, Germany
[c] Department of Psychiatry, Psychotherapy and Psychosomatics, RWTH Aachen University, Aachen, Germany
[d] Department of Investigative Radiology, National Cerebral and Cardiovascular Center Research Institute, 5-7-1, Fujishirodai, Suita, Osaka 565-8565, Japan

ARTICLE INFO

Article history:
Received 30 September 2012
Revised 28 November 2012
Available online 10 December 2012

Keywords:
Ultra high-field MRI
Magnetic resonance imaging
Hybrid imaging
Multi-modal imaging
MR–PET
PET/MR
PET
Positron emission tomography
High resolution imaging
Metabolic imaging
Sodium imaging
EEG–fMRI
MR–PET–EEG

ABSTRACT

Multi-modal MR–PET–EEG data acquisition in simultaneous mode confers a number of advantages at 3 T and 9.4 T. The three modalities complement each other well; structural–functional imaging being the domain of MRI, molecular imaging with specific tracers is the strength of PET, and EEG provides a temporal dimension where the other two modalities are weak. The utility of hybrid MR–PET at 3 T in a clinical setting is presented and critically discussed. The potential problems and the putative gains to be accrued from hybrid imaging at 9.4 T, with examples from the human brain, are outlined. Steps on the road to 9.4 T multi-modal MR–PET–EEG are also illustrated. From an MR perspective, the potential for ultra-high resolution structural imaging is discussed and example images of the cerebellum with an isotropic resolution of 320 μm are presented, setting the stage for hybrid imaging at ultra-high field. Further, metabolic imaging is discussed and high-resolution images of the sodium distribution are presented. Examples of tumour imaging on a 3 T MR–PET system are presented and discussed. Finally, the perspectives for multi-modal imaging are discussed based on two on-going studies, the first comparing MR and PET methods for the measurement of perfusion and the second which looks at tumour delineation based on MRI contrasts but the knowledge of tumour extent is based on simultaneously acquired PET data.

1. Introduction

Tomographic imaging methodologies are essentially focused on the generation of tissue contrast in a given plane of interest. Contrast between different tissues arises from the differences in endogenous physical properties or through the introduction of exogenous "contrast agents". Often a single contrast, or multiple contrasts from the same imaging modality, simply do not suffice to enable a complete diagnostic decision to be reached or, in scientific studies, leave aspects of the question unanswered. As such, a desire to address the same problem in different imaging machines arises. Specifically, spatial co-localisation of the information from the different modalities might be desired or indeed, the introduction of a temporal dimension might be required.

Magnetic resonance imaging (MRI) is characterised by its excellent tissue contrast based on, for example, T_1 and T_2 relaxation times, proton density, and diffusion/flow properties. Due to this fact, it has been widely used for structural/diagnostic imaging in the clinic and also for functional brain imaging in neuroscientific research.

Positron emission tomography (PET) is a widely used and well-established tool for clinical tumour diagnostics and is the gold standard for metabolic imaging. In contrast to MRI, PET provides insights into physiological and pathophysiological processes, albeit at a comparatively low anatomical resolution. Consequently, as shown here in an example from brain tumour imaging (see below), PET can be seen as an outstanding complement to MRI with respect to its metabolic specificity and its ability to enable tumour differentiation and tumour extent mapping [1].

Recently, two major developments in the fields of MRI and PET have taken place. In the MRI domain, the field strength of scanners for human application has moved to the ultra-high field range of

* Corresponding author at: Institute of Neuroscience and Medicine-4, Research Centre Jülich, 52425 Jülich, Germany.
E-mail address: n.j.shah@fz-juelich.de (N.J. Shah).

1090-7807/$ - see front matter © 2012 Elsevier Inc. All rights reserved.
http://dx.doi.org/10.1016/j.jmr.2012.11.027

up to 9.4 T and even beyond. Ultra-high fields facilitate structural imaging with significantly higher spatial resolution, higher functional (BOLD) contrast [2], perhaps even at the level of columnar resolution, and enhanced image contrast [3]. Moreover, such ultra-high field MRI scanners open up the opportunity to perform non-proton MRI and spectroscopy with a reasonable, PET-like spatial resolution in the order of 3 mm isotropic [4–6].

Regarding the use of PET in the MRI environment, the use of photo multiplier tubes (PMTs), that are extremely sensitive to magnetic fields, has been abandoned in favour of avalanche photo diodes (APDs) that are field insensitive. The implementation of new detector technologies based on APDs has led to true hybrid MR–PET scanners, capable of simultaneous MRI and PET data acquisition and has thus negated the need to perform scans in two separate machines. These hybrid scanners have the advantage of measuring PET and MRI datasets that are intrinsically co-registered in time and space [7–9]. Furthermore, inclusion of a PET scanner inside an MRI system brings with it advantages for PET image reconstruction. Partial volume correction, attenuation and motion correction can be performed based on MRI images acquired simultaneously with the PET data. In particular, clinical applications and neuroscientific research will benefit from these recent developments in terms of opportunities for metabolic imaging, accurate receptor density mapping, and novel paradigms for brain function.

In the confines of this article, multimodal imaging is defined as the summation of information from different imaging modalities whereby it is noted that MRI could well be regarded as being inherently multimodal, given the plethora of contrast mechanisms that can be exploited to generate image contrast. The combination of MRI and PET will be discussed; the measurement of MRI and PET data in two separate scanners will not be addressed and attention will instead be focused on hybrid MR–PET scanners studying the human brain and that are capable of the acquisition of simultaneous datasets. Hybrid MR–PET data acquisition at 3 T and at 9.4 T in humans will be explored. Further, the additional introduction of a temporal dimension, in the form of electroencephalography (EEG), in hybrid mode, will also be presented and discussed. Multimodal imaging in the form of simultaneous MR–EEG, and the extension thereof to triple modality MR–PET–EEG will also be briefly presented; the rationale for triple modal imaging is presented in Fig. 1 in the form of "finger print" diagrams.

2. Hybrid MR–PET scanner construction

The prototype 3 T MR–PET scanner used to obtain the results described herein comprises a commercially-available 3 T Siemens Tim Trio MR system and a custom-built BrainPET insert designed especially for brain imaging (Siemens Healthcare, Erlangen, Germany). The 9.4 T hybrid is also a Siemens prototype system based around a magnet with a warm-bore diameter of 90 cm and a PET insert that is nearly identical to that of the 3 T scanner. The BrainPET insert (Fig. 2) is a compact cylinder (length of 72 cm and an outer diameter of 60 cm) consisting of 32 copper-shielded detector cassettes each with six detector modules. The diameter of the PET field-of-view is 31.4 cm and 19.2 cm in the axial direction. The front end of the detector module is a 12×12 matrix of individual lutetium oxyorthosilicate (LSO) crystals coupled to a 3×3 array of APDs thus rendering the detector insensitive to the magnetic field of the MR system. The small volume of the LSO crystals measuring $2.5 \times 2.5 \times 20\ mm^3$ leads to a central PET image resolution of about 3 mm [10]; this is one of the best spatial resolutions for

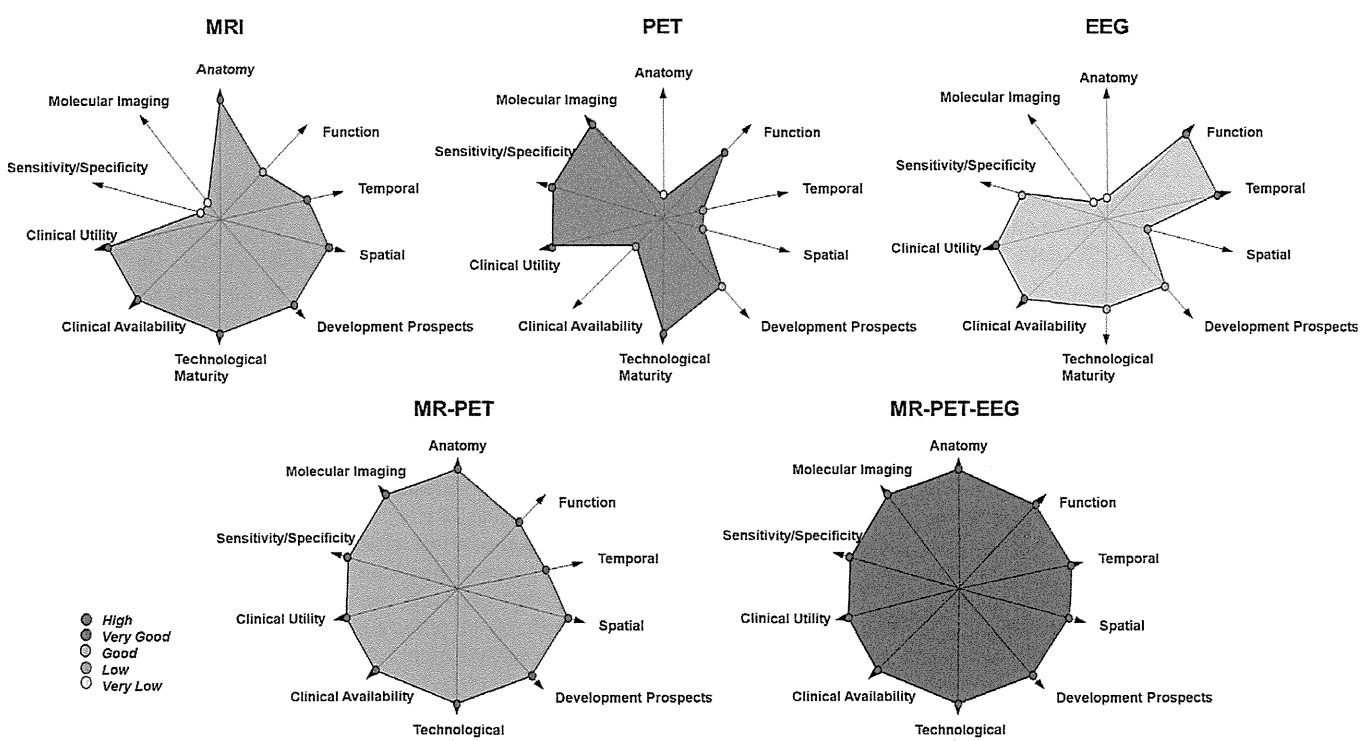

Fig. 1. Fingerprint diagrams giving an overview of the strengths of MRI, PET and hybrid MR–PET, and hybrid MR–PET–EEG. Starting at the origin, the further one traverses along a given axis, the better that particular attribute is fulfilled. MRI can provide exquisite spatial resolution and the technology is widely available. However, MRI is not strong in the area of molecular imaging and its specificity is also somewhat limited. PET on the other hand, has poorer spatial and temporal resolution than MRI but it is extremely specific – an attribute conferred upon it by the choice of radiolabelled tracer – and is also very sensitive. Both MRI and PET have a poor temporal resolution regarding mapping of brain function, for example. In a hybrid scanner capable of simultaneous measurement of all three dataset, all the chosen attributes are fulfilled in entirety.